Article

Site-Selective Growth of AgPd Nanodendrite-Modified Au Nanoprisms: High Electrocatalytic Performance for CO2 Reduction
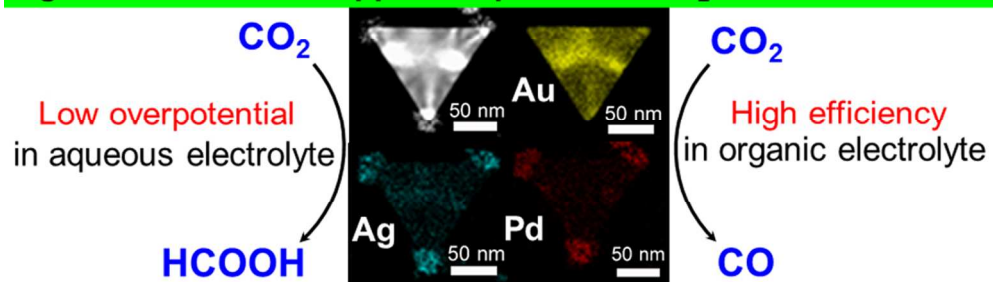
Changsheng Shan, Erin T. Martin, Dennis G Peters, and Jeffrey M. Zaleski

Just Accepted

1
2
3
4
5
6
7
8
9
10
11
12
13
14
15
16
17
18
19
20
21
22
23
24
25
26
27
28
29
30
31
32
33
34
35
36
37
38
39
40
41
42
43
44
45
46
47
48
49
50
51
52
53
54
55
56
57
58
59
60

88x29mm (300 x 300 DPI)

Site-Selective Growth of AgPd Nanodendrite-Modified Au Nanoprisms: High Electrocatalytic Performance for CO$_2$ Reduction

Changsheng Shan[‡], Erin T. Martin[‡], Dennis G. Peters*, and Jeffrey M. Zaleski*

Indiana University, Department of Chemistry, Bloomington, IN 47405

[‡]These authors contributed equally to the work.

*Email: zaleski@indiana.edu; peters@indiana.edu.

Abstract

Environmental impacts of continued CO$_2$ production have led to an increased need for new methods of CO$_2$ removal and energy development. Nanomaterials are of special interest for these applications, due to unique chemical and physical properties that allow for highly active surfaces. Here, we successfully synthesize AgPd nanodendrite-modified Au nanoprisms in various shapes (nanoprisms, hexagonal nanoplates, and octahedral nanoparticles) by selective metal deposition. This strategy involves coupling galvanic replacement between Ag layers in Au@Ag core-shell nanoprisms and H$_2$PdCl$_4$ with a co-reduction process of silver and palladium ions. Synthesis of AgPd nanodendrite-tipped (4.14–11.47 wt% Pd) and -edged (25.25–31.01 wt% Pd) Au nanoparticles can be controlled simply by a tuning of the concentration of H$_2$PdCl$_4$. More importantly, these multi-component AgPd nanodendrite-modified Au nanoparticles show exceptional electrocatalytic performance for CO$_2$ reduction. AgPd nanodendrite-edged Au nanoprisms show more favorable potentials (–0.18 V vs. RHE) than previously reported nanocatalysts for the reduction of CO$_2$ to formate, and exhibit

higher faradaic efficiencies (49%) than Au, Au@Ag, and AgPd nanodendrite-tipped Au nanoprisms in aqueous electrolytes. Moreover, AgPd nanodendrite-modified Au nanoprisms show much higher selectivity and faradaic efficiency for CO_2 reduction to CO (85–87%) than Au and Au@Ag nanoprisms (43–64%) in organic electrolytes. The high performance of these particles for CO_2 reduction is attributed to the unique structure of AgPd nanodendrite-modified Au nanoprisms and the synergistic effect of Ag having an affinity for CO_2, efficient binding of hydrogen at Pd, and Au as a stable, conductive support. In addition, AgPd nanodendrite-edged Au nanoprisms show highly stable catalytic activity during long-term electrolyses (up to 12 h) and repetitive use. These exciting results indicate that AgPd nanodendrite-modified Au nanoparticles are promising for application in CO_2 conversion into useful fuels.

Introduction

Continued consumption of fossil fuels worldwide has led to two vital concerns: development of new energy resources and mitigation of the environmental impacts of CO_2 production.[1-6] Advances in sustainable energy and pollution control include the capture and conversion of CO_2 into reusable forms. A variety of methods exists for the harnessing of CO_2 and for its conversion to usable fuels, including chemical reactions,[7] photocatalysis,[8,9] and electrocatalysis.[10-13] Of these, electrocatalysis exhibits several distinct advantages; the ability to control reaction products through choice of solvent, electrode material, and applied potential, minimization of waste and byproducts, and

2

generally mild reaction conditions make electrochemical treatment of CO_2 an attractive option.[10,14]

Despite the appeal of electrochemical methods, achieving effective reduction of CO_2 comes with its own challenges. Electrochemical CO_2 reduction often suffers from high overpotentials, requiring large amounts of energy, as well as poor efficiency in the presence of competing reactions such as hydrogen evolution and solvent–electrolyte breakdown. To control reaction pathways and to decrease the overpotential of CO_2 reduction, unique electrocatalytic materials have been designed, often on the nanoscale in order to maximize active sites.[15-19] Metal nanocatalysts have been extensively studied, including Au nanoparticles,[15,20] Ag nanoparticles,[21] nanoporous Ag,[22] Pd nanoparticles,[23] and Au/Cu nanoparticles,[24] but concerns of overpotential, selectivity, and catalyst stability still exist.

When new electrocatalysts for CO_2 reduction are designed, choice of material and structure is paramount. Recent advances in nanomaterial synthesis have led to the development of heterogeneous metal nanoparticles with exciting catalytic properties, whose large areas, sharp tips, and metal coupling allow for wide application in catalysis and sensing.[25-28] Many heterogeneous metal nanoparticles are reported as core–shell structures, which block the functionality of the inner metal core.[29-32] Other heterogeneous metal nanoparticles have special spatial arrangements, such as nanoframes, nanodendrites, or site-selective deposition of metals on the metal cores, which show high catalytic properties.[27,33-40] In addition, metal nanoparticles with nanodendritic structures have shown high catalytic properties due to larger surface areas

3

and more active sites.[37,41] Therefore, heterogeneous nanomaterials with nanodendritic structures are particularly promising for catalysis due to a high number of active sites and access to multiple metals at the surface. To our knowledge, there are only a few reports for the successful synthesis of symmetrical, multi-branched heterogeneous structures due to varying reduction rates of metal ions, galvanic replacement, and the thermodynamic miscibility of metal phases.[27,28] Therefore, controlled growth of multi-branched heterogeneous structures still presents a challenge.

Here, we develop a facile method for site-selective growth of AgPd nanodendrite-modified Au nanoarchitectures of different geometries for electrochemical CO_2 reduction. Au@Ag core-shell nanoparticles undergo galvanic replacement in the presence of H_2PdCl_4 and subsequent co-reduction and deposition of silver and palladium. We control site-selectivity of this co-deposition by varying Ag and H_2PdCl_4 content, resulting in Au nanoparticles edged or tipped with AgPd nanodendrite structures. The activity of these nanomaterials toward CO_2 reduction is explored by cyclic voltammetry in both aqueous and organic solvents, and remarkably favorable reduction potentials at nanodendrite-edged and -tipped nanoprisms are observed. The efficiency of these nanoprisms (Au, Au@Ag, AgPd nanodendrite-modified Au) for bulk CO_2 reduction is analyzed through controlled-potential electrolyses, and reduction products are identified by means of gas chromatography and NMR measurements. Faradaic efficiencies for the production of formic acid, CO, and oxalic acid are reported, and mechanistic schemes are proposed for the reduction of CO_2 at these novel nanodendrite-modified catalysts.

4

Experimental

Reagents.

Hydrogen tetrachloroaurate trihydrate (HAuCl$_4$•3H$_2$O, 99.9%), silver nitrate (AgNO$_3$, 99%), palladium chloride (PdCl$_2$, 99%), sodium citrate (99%), L-ascorbic acid (AA, 99%), sodium borohydride (NaBH$_4$, 98%), sodium iodide (99.5%), sodium hydroxide (NaOH, 98%), and hexadecyltrimethylammonium bromide (CTAB, ≥99%) were all purchased from Sigma–Aldrich and used as received. Hexadecyltrimethylammonium chloride (CTAC, >95%) was purchased from Tokyo Chemical Industry Co., Ltd. (TCI) and used without further purification. Millipore ultra-filtered water (18 MΩ•cm) was used for all aqueous preparations. For electrochemical measurements, each of the following chemicals (with purity given in parentheses) was purchased from Sigma–Aldrich, or from a different commercial source when indicated, and was used as received: carbon dioxide (Airgas, bone-dry grade), carbon monoxide (Airgas, 2000 ppm in N$_2$), formic acid (J. T. Baker, 90%), oxalic acid (98%), glyoxylic acid monohydrate (98%), glycolic acid (98%), *n*-hexadecane (99%), deuterium oxide (D$_2$O, 99.9 atom % D), N,O-bis(trimethylsilyl)trifluoroacetamide with 1% trimethylchlorosilane (BSTFA:TCMS, Supelco, 99.5%), and 3-(trimethylsilyl)-1-propanesulfonic acid sodium salt (97%). Purified water (Omnisolv, HPLC grade) and acetonitrile (ACN, Omnisolv, 99.9%) were used as solvents for electrochemical experiments. Tetramethylammonium tetrafluoroborate (TMABF$_4$, TCI, 98%), employed as supporting electrolyte in organic solvents, was recrystallized from a

5

mixture of ethanol and water, then subsequently stored in a vacuum oven at 80 °C for

48 h to remove traces of water. Lithium perchlorate (GFS Chemicals, reagent grade)

was employed as supporting electrolyte for aqueous solvents and used as received.

Deaeration of all solutions was accomplished with the aid of UHP-grade argon (Airgas).

Characterization of materials.

Transmission electron microscopy (TEM) was performed with a JEOL 1010

microscope operating at 80 kV. High-resolution transmission electron microscopy

(HRTEM), scanning transmission electron microscopy (STEM), and energy-dispersive

X-ray spectroscopy (EDX) data were collected on a JEOL JEM 3200FS instrument at

300 kV accelerating voltage. Scanning electron microscopy (SEM) and EDX data were

obtained by means of the SEM mode of a focused ion-beam instrument (Zeiss, Auriga

60) with EDX spectroscopy accessories. UV-Vis-NIR measurements were collected

with a Varian Cary 5000 spectrometer.

Synthesis of Au, Au@Ag, and Au/AgPd nanoprisms

 Synthesis of Au nanoprisms. Gold (Au) nanoprisms were synthesized by the

three-step seed-mediated method reported previously.[42,43] First, Au nanoparticle seeds

were prepared by reduction of $HAuCl_4$ with $NaBH_4$. An aqueous solution of $NaBH_4$ (1

mL, 100 mM, ice-cold water) was quickly added into a mixing solution containing 37

mL of deionized water, 1 mL of 10 mM aqueous sodium citrate, and 0.33 mL of 30 mM

$HAuCl_4$, while being stirred vigorously. After 1 min, the resulting seed solution was

6

aged for 2–3 h to allow hydrolysis of unreacted NaBH$_4$. Following the aging period, a growth solution containing 108 mL of 0.05 M CTAB, 22 µL of 0.1 M NaI, 3 mL of 10 mM HAuCl$_4$, 0.6 mL of 0.1 M NaOH and 0.6 mL of 0.1 M AA was divided into three aliquots for the seed-mediated growth step. The first two solutions (solution 1 and solution 2) contained 9 mL of the above growth solution, whereas solution 3 contained the remaining 94 mL of growth solution. Nanoprism formation was initiated by fast addition of 1 mL of seed solution to growth solution 1, and the mixture was shaken for 5 s. One mL of resulting solution 1 was then immediately added to solution 2 and shaken for 5 s. The total contents of solution 2 were immediately added to solution 3 and shaken for 5 s. After this addition, the final solution changed from colorless to deep magenta and was kept undisturbed overnight. Nanoprisms precipitated on the bottom of the flask were collected by removal of the supernatant. Collected nanoprisms were redispersed in 20 mL of aqueous 0.05 M CTAB solution.

Synthesis of Au@Ag core-shell nanoprisms. Au@Ag core-shell nanoprisms were synthesized by means of a modified method from the literature.[30] CTAB (9 mL, 0.05 M), AA (0.4 mL, 0.1 M), and NaOH (0.6 mL, 0.1 M) were added to 3 mL of a previously prepared suspension of Au nanoprisms. Aqueous AgNO$_3$ solution (3.5 mL, 1 mM) was added with stirring to the above mixture at a rate of 160 µL/min with a mechanical syringe pump (KD Scientific 200). After addition of AgNO$_3$, the resulting Au@Ag core-shell nanoprisms were centrifuged at 7000 rpm for 10 min and then re-dispersed in 3 mL of 0.05 M CTAB. These Au@Ag nanoprisms were grown further by a single repetition of the above method, to yield a moderate coating of Ag, or 4

7

repetitions, to produce nanoprisms with a higher Ag coating. A third set of Au@Ag

nanoprisms was created with a low Ag coating by use of only 0.6 mL of 1 mM $AgNO_3$

in a single step.

Synthesis of AgPd nanodendrite-tipped and -edged Au nanoprisms. AgPd

nanodendrite-tipped and -edged Au nanoprisms were prepared by addition of AA

solution and H_2PdCl_4 solution to 1 mL of the previously prepared Au@Ag

nanoprisms.[34] Four different solutions were prepared containing 5, 10, 25, or 100 µL

of 2 mM AA. The volume of 2 mM H_2PdCl_4 solution used was twice that of the AA

solution in each case. Resulting solutions were left undisturbed at room temperature

for 3 h, then centrifuged at 7000 rpm for 10 min, washed with water once, and

redispersed in 100 µL of water. The nanoprism coating morphology depends on the

ratio of substrates used; the above procedure yields both tipped and edged nanoprisms.

Synthesis of Au, Au@Ag, Au/AgPd hexagonal nanoplates

Synthesis of Au hexagonal nanoplates.   Synthesis of Au and Au@Ag

hexagonal nanoplates was accomplished according to the modified method.[44] Au

nanoprisms, synthesized by the previously described method, provided seeds to grow

Au hexagonal nanoplates. AA (22.5 mL, 4.73 mM) was added with stirring to a mixture

containing 65 mL of 0.05 mM CTAB, 37.5 µL of 0.1 M NaI, 2 mL of 30 mM

$HAuCl_4 \cdot 3H_2O$, and 10 mL of the Au nanoprism suspension at a rate of 0.5 mL/min by

means of a mechanical syringe pump (KD Scientific 200). After 3 h, the synthesized

8

hexagonal nanoplates were collected by centrifugation at 3000 rpm for 10 min and redispersed in 100 mL of 0.05 M CTAB.

Synthesis of Au@Ag hexagonal nanoplates. A growth solution containing 6 mL of 0.05 mM CTAB, 400 µL of 0.1 M AA, 600 µL of 0.1 M NaOH, and 3.2 mL of 1 mM AgNO$_3$ was added to 6 mL of the previously prepared hexagonal nanoplate suspension and vigorously stirred for 30 min. Then the resulting Au@Ag core-shell nanoplate suspension was centrifuged at 3000 rpm for 10 min, and the product redispersed in 6 mL of 0.05 M CTAB. Au@Ag nanoplates were grown further by one-time repetition of the above growth method. Final Au@Ag core-shell hexagonal nanoplates were dispersed in 12 mL of water.

Synthesis of AgPd nanodendrite-tipped and -edged Au hexagonal nanoplates. AgPd nanodendrite-tipped and -edged Au hexagonal nanoplates were synthesized by the same procedure as AgPd-modified Au nanoprisms. AA (25 µL, 2 mM) and H$_2$PdCl$_4$ (50 µL, 2 mM) were added sequentially to 1 mL of previously prepared Au@Ag core-shell hexagonal nanoplate suspension to obtain AgPd nanodendrite-tipped Au hexagonal nanoplates. Resulting mixtures were left undisturbed at room temperature for 3 h, then centrifuged at 3000 rpm for 10 min, washed with water once, and redispersed in 100 µL of water. Au@AgPd-edged hexagonal nanoplates were prepared by the same method, except that 100 µL of 2 mM AA and 200 µL of 2 mM H$_2$PdCl$_4$ were used.

9

Synthesis of Au, Au@Ag, AgPd nanodendrite-tipped and -edged octahedral nanoparticles

Synthesis of Au octahedral nanoparticles. Gold (Au) octahedral nanoparticles were synthesized according to Huang's method.[45,46] A gold seed solution was prepared by fast addition of 0.45 mL of ice-cold 0.02 M $NaBH_4$ to a mixture of 10 mL of deionized water and 80 µL of 30 mM $HAuCl_4$. After being stirred for 1 min, the seed solution was aged for 1 h at 30 ℃ in a water bath to decompose unreacted $NaBH_4$. Two growth solutions (1 and 2) were then prepared. First, CTAC surfactant (0.32 g) was dissolved in 9.6 mL water. Subsequently, 80 µL of 30 mM $HAuCl_4$, 5 µL of 10 mM KI, and 220 µL of 40 mM AA were added. Next, Au seed solution (25 µL) was added to solution 1 and shaken for 5 s. The resulting solution 1 (25 µL) was then added quickly to solution 2 and shaken for 10 s. Solution 2 was left undisturbed for 15 min to allow for particle growth, then centrifuged at 7000 rpm for 10 min. The final octahedral nanoparticles were redispersed in 10 mL of aqueous 0.05 M CTAB solution.

Synthesis of Au@Ag octahedral nanoparticles. Synthesis of Au@Ag octahedral nanoparticles was similar to that of Au@Ag nanoprisms, except that a suspension of Au octahedral seeds was used instead of Au nanoprisms. With stirring, $AgNO_3$ (3.5 mL, 1 mM) was added to a mixture of 3 mL of Au octahedral seed suspension, 9 mL of 0.05 M CTAB, 0.4 mL of 0.1 M AA, and 0.6 mL of 0.1 M NaOH at a rate of 160 µL/min by means of a mechanical syringe pump. After addition of $AgNO_3$, the resulting Au@Ag core-shell octahedral nanoparticles were centrifuged at 7000 rpm for 10 min and then redispersed in 6 mL of water.

Synthesis of AgPd nanodendrite-tipped and -edged Au octahedral nanoparticles. We prepared AgPd nanodendrite-tipped and -edged Au octahedral nanoparticles by the same procedure as the AgPd nanodendrite-tipped and -edged Au hexagonal nanoplates, except for substitution of Au hexagonal nanoplate seeds by Au octahedral nanoparticles. Resulting mixtures were left undisturbed at room temperature for 3 h, then centrifuged at 7000 rpm for 10 min, washed with water one time, and redispersed in 100 µL water.

Electrochemical cells, electrodes, instrumentation, and procedures

Cyclic voltammetry. For cyclic voltammetry experiments, a Princeton Applied Research Corporation (PARC) model 2273 or 273A potentiostat was used with PowerSuite® software. Cells and procedures used have been described in previous publications.[47,48] To prepare nanomaterial electrode surfaces, 10 µL of a nanomaterial slurry was drop-cast onto a glassy carbon disk (Grade GC-20, 3.0-mm-diameter, Tokai Electrode Manufacturing Company, Tokyo, Japan), which was press-fitted into a Teflon rod to yield a geometric area of 0.071 cm^2. These electrodes were immersed in deaerated aqueous solvent–electrolyte with a platinum coil counter electrode and a saturated calomel reference electrode, and cleaned by means of repeated cycling of the potential between 0 and –1 V at a scan rate of 20 mV s^{-1}. In organic solvent, the reference electrode consisted of a cadmium-saturated mercury amalgam in contact with DMF saturated with both sodium chloride and cadmium chloride; this electrode has a potential of –0.76 V versus the aqueous saturated calomel electrode (SCE) at 25 °C.[49-

[51] Geometric current densities were determined on the basis of the known surface area of the glassy carbon support.

Controlled-potential electrolyses. Bulk electrolyses were performed with the aid of a PARC model 173 potentiostat. A locally written LabView program was used for data collection, and the acquired data were processed with OriginPro 2015 software. A two-compartment (divided) cell, described elsewhere,[52] was modified to hold a wax-impregnated graphite electrode (WIGE) prepared in-house. This working electrode, with a geometric area of 0.28 cm^2, was modified by means of drop-casting 40 µL of a nanomaterial slurry onto the working surface. Either a saturated calomel or cadmium amalgam reference electrode was also present in the cathode compartment of the cell, which was separated from the anode compartment by a sintered-glass disk and agar or methyl cellulose plug. A carbon rod served as an auxiliary anode. Due to the volatility of products arising from the reduction of carbon dioxide, sparging of argon through the cathode compartment to remove oxygen was terminated as soon as the background current reached a baseline level at the chosen potential, whereupon the cell was saturated with carbon dioxide and sealed. Electrolyses performed in water lasted 2–6 h, whereas electrolyses in organic solvent typically lasted 45 min. Additional experiments were performed at longer times under a constant flow of CO_2 to analyze catalyst stability. In all cases, geometric current densities with respect to the area of the graphite support were reported as average current passed over the time of the electrolysis. Only current passed after introduction of CO_2 to the cell was included in these calculations, eliminating the contribution of background processes that occur

12

during the pre-electrolysis step. Additionally, SEM images of the tip of a modified

electrode, which was cut with a razor from the graphite rod support, were obtained

before and after electrolysis. TEM images of nanomaterial catalyst removed from the

graphite support by sonication (10 s) in water were also obtained for comparison.

Electrolysis product analysis. Identification and quantitation of formic acid

was achieved by means of nuclear magnetic resonance (NMR) experiments. After an

electrolysis, the catholyte was diluted with deuterium oxide and 3-(trimethylsilyl)-1-

propanesulfonic acid sodium salt was added as an internal standard. Samples were

analyzed with a Varian 600-MHz spectrometer equipped with a cryogenic probe, and

data were processed with MestReNova software. Integration of formic acid and internal

standard peaks allowed for quantitative results as outlined in the literature.[53]

Other products were detected by means of gas chromatography. For

quantitation of carbon monoxide, an Agilent Technologies 6890N gas chromatograph

fitted with an HP-PLOT Molesieve/5A column and a thermal conductivity detector

(TCD) were used with helium as a carrier gas. A gas-tight syringe was used to sample

the headspace of the electrochemical cell, and 0.50 mL of gas was injected directly onto

the column. Quantitation of carbon monoxide was achieved by means of a calibration

curve. Oxalic, glyoxylic, and glycolic acid were derivatized before analysis. Catholyte

was concentrated and treated with an equal volume of BSTFA:TCMS, then heated at

60 °C for one hour to prepare the respective trimethylsilyl derivatives. Detection of

these derivatives was accomplished with the aid of an Agilent 6890N gas

chromatograph fitted with a 30 m $\times$ 0.32 mm capillary column (J & W Scientific) that

13

had a DB-5 stationary phase consisting of 5% phenylpolysiloxane and 95% methylpolysiloxane and a flame ionization detector (FID). Internal standard (*n*-hexadecane) was added for quantitation purposes; to determine gas chromatographic response factors, a mock cell containing anticipated concentrations of products and internal standard was allowed to stir (without application of a potential) for the same length of time as an actual bulk electrolysis. Response factors and chromatographic peak areas were measured with the aid of Agilent Chemstation software, and used to determine product distributions according to a previously developed procedure.[54]

In all cases, faradaic efficiencies were calculated by comparison of total charge passed during an electrolysis and the actual charge needed to produce detected quantities of products according to known electrochemical mechanisms.

Results and Discussion

Synthesis and Characterization of Nanoprisms. AgPd nanodendrite-modified Au nanoprisms were synthesized by the coupling of galvanic replacement between H_2PdCl_4 and the Ag layers of Au@Ag core-shell nanoprisms with a co-reduction process that used ascorbic acid (AA) as the reductant (Scheme 1). First, Au@Ag nanoprisms were synthesized by slow addition of 1 mM $AgNO_3$ to a mixture containing AA, NaOH, and Au nanoprisms with an average edge length and thickness of 154.0 ± 8.4 nm and 8.3 ± 1.1 nm, respectively (Figures 1A, S1A). The resulting Au@Ag nanoprisms have an Au:Ag ratio of 1:3, an average edge length of 200 ± 23 nm, and an average thickness of 23.4 ± 3.7 nm (Figures 1B, S1C); the larger size of these prisms is

14

a result of the added Ag layer. Prominent features from Au and Ag in the EDX spectra of Au@Ag nanoprisms (Figure S2) clearly indicate the successful deposition of Ag layers on the Au nanoprisms. Au@Ag nanoprisms were further modified by addition of H_2PdCl_4 to produce AgPd nanodendrite-modified Au nanoprisms. TEM and HRTEM images show that AgPd deposits on prism edges (Figures 1C, S3) and tips (Figures 1D–F) are composed of numerous dendrite nanocrystals with average sizes of 6.9 ± 1.0 nm on the edges and 6.5 ± 1.2 nm at the tips. In Figure 1F, observed lattice d-spacings corresponding to the (111) and (200) planes of AgPd nanoparticles are located between of the (111) and (200) planes of metallic Ag and Pd nanoparticles,[55-57] indicating the formation of AgPd alloy nanoparticles.

Nanoprisms were further characterized by means of UV-Visible-NIR measurements. A solution of Au nanoprisms exhibits two peaks at 790 nm and 1280 nm (Figure S4), corresponding to dipole and quadrupole surface plasmon resonances (SPRs), respectively, which are consistent with previous reports.[42,43] After deposition of Ag layers to form Au@Ag nanoprisms, a new longitudinal dipole plasmon resonance is observed at 870 nm.[58-61] Additionally, two plasmon resonance peaks are observed at 545 nm and 340 nm; these correspond to in-plane quadrupole resonance and out-of-plane quadrupole resonance of Ag nanoprisms, respectively.[61] These results indicate the successful formation of Au@Ag nanoprisms. After galvanic reaction of the Ag layer with H_2PdCl_4, these features red shift to 1312 nm and 1330 nm, indicating the disappearance of Ag layers and the formation of AgPd nanodendrite-modified Au nanoprisms.

15

Structures and compositions of AgPd nanodendrite-modified nanoprisms were further confirmed by STEM/EDX, XRD, and SEM/EDX spectroscopy. STEM and EDX-mapping images show the triangular Au core and well-defined AgPd nanodendrite-tipped (Figures 2A−D) as well as AgPd nanodendrite-edged structures (Figures 2F−I). The uniformly dispersed signals of Ag and Pd in overlay images (Figures 2E, 2J) indicate the AgPd alloyed nanostructure, which is further confirmed by XRD. XRD patterns of Au and Au@Ag nanoprisms clearly show four diffraction peaks at ca. $2\theta = 38.3$, 44.5, 64.7, and 77.7, which can be indexed to (111), (200), (220), and (311) facets of face-centered-cubic (*fcc*) metal, respectively (Figure S5). Compared to Au and Au@Ag nanoprisms, the AgPd nanodendrite-tipped Au nanoprisms show relatively wider peaks with a small blue shift, which is attributed to the formation of AgPd nanodendrites. With more AgPd nanodendrites, the AgPd nanodendrite-edged Au nanoprisms show diffraction peaks from both Au nanoprisms and AgPd nanodendrites. Notably, peaks observed for AgPd nanodendrites are located between those of Pd (JCPDS-46-1043) and Ag (JCPDS-04-0783), suggesting an AgPd alloy.

Content of Pd, Ag, and Au for each type of nanoprism were determined from EDX spectra and found to be 8.80, 63.63, and 27.57 wt% for AgPd nanodendrite-tipped nanoprisms (Figure S6A, B) and 25.51, 46.08, and 28.41 wt% for AgPd nanodendrite-edged nanoprisms (Figure S6C, D), respectively. All above results indicate the successful formation of AgPd nanodendrite-modified Au nanoprisms.

Controlled synthesis of AgPd nanodendrite-modified Au nanoprisms. Site-selective growth of AgPd nanodendrites on Au nanoprisms is dependent on both the

16

amount of Ag coating and the concentration of H_2PdCl_4 used for the galvanic replacement step. With a low ratio of Ag to Au of 1:3 in the core-shell nanoprisms (Figures 3A, S2A), only AgPd nanodendrite-edged Au nanoprisms are produced, even in the presence of different amounts of H_2PdCl_4 (Figures 3B–E). At higher coatings of Ag with ratios of Ag:Au of 3:1 (Figures 3F, S2B), both AgPd nanodendrite-tipped and -edged prisms are formed depending on the concentration of H_2PdCl_4 (Figures 3G–J); increasing the concentration of H_2PdCl_4 leads from nanodendrite-tipped structures to nanodendrite-edged structures. Similar results are observed for an Ag:Au ratio of 10:1 (Figures 3K–O, S2C).

The effects of Ag content and H_2PdCl_4 concentration on structure follow from the basic principle of this synthetic method: galvanic replacement of the Ag layer in Au@Ag nanoprisms with H_2PdCl_4 and co-reduction of H_2PdCl_4 and Ag^+ ions, generated from the galvanic replacement reaction, at specific sites on nanoparticle seeds. Reactivity of these sites varies; for example, Mulvaney and coworkers have shown that high curvature sites on Au nanorods are the most reactive, due to a high rate of collisions between these sites and micelles containing metal ions.[62] In the case of nanoprisms, Pd and Ag are expected to co-deposit favorably on high curvature sites at edges and tips. Selectivity of these sites can also be tuned if one controls the rate of the galvanic replacement reaction, in which the Ag layer, first formed by underpotential deposition (UPD) of Ag on Au,[63,64] is oxidized in the presence of Pd^{2+} to release Ag^+ ions and to create an excess of electrons on the particle surface. Electrons generated by this reaction accumulate at regions of high curvature,[65-69] resulting in preferential

17

reduction of Pd^{2+} ions and subsequent co-deposition of Pd and Ag metal on tips and edges. A slow rate of galvanic replacement, and thus limited generation of electrons, allows accumulation in only the regions of highest curvature, the tips of nanoparticle seeds. For this reason, particle synthesis with low concentrations of H_2PdCl_4 results only in nanodendrite-tipped materials. Faster reaction rates will produce an overabundance of electrons, resulting in a wider dispersion of charge and accumulation at both tips and edges, allowing formation of both nanodendrite-tipped and −edged materials.[64]

Formation of AgPd nanodendrite-modified Au nanoprisms follows the above trend. When the Ag content of the Au@Ag nanoprism is high enough to support continuous reaction (Ag:Au ratios of 3:1 and 10:1), the type of nanoprism formed is dependent on the concentration of H_2PdCl_4 present. Low availability of Pd^{2+} in solution (less than 50 μL of 2 mM H_2PdCl_4) results in a slow galvanic reaction rate and limited generation of electrons and Ag^+ ions, allowing for migration of charge to the nanoprism tips and subsequent deposition of Pd and Ag (Figures 3G–I, K–N). At higher concentrations (200 μL of 2 mM H_2PdCl_4), electrons are quickly consumed at tip sites, leaving excess Pd^{2+} and Ag^+ ions to be reduced along available, electron-saturated edge sites (Figures 3J, O). However, when the ratio of Ag:Au is low (1:3), even low concentrations of Pd^{2+} overwhelm the Ag layer of the nanoprism. Fast consumption of electrons does not allow for migration and accumulation of charge (electrons and Ag^+) at nanoprism tips, resulting in the exclusive formation of nanodendrite-edged nanoprisms regardless of initial H_2PdCl_4 concentration (Figures 3B–E).

18

These site-selective strategies can be further applied to Au nanoparticle cores with other shapes, such as hexagonal nanoplates and octahedral nanoparticles. Au, Au@Ag, AgPd nanodendrite-tipped and -edged Au nanoplates (Figures S7A–D, S8A–B, S9A, S9C) and octahedral nanoparticles (Figures S7E-H, S10, S11A, S11C) were characterized with the aid of TEM and SEM. Specific metal contents of Ag, Pd and Au in these Au@Ag and AgPd nanodendrite-modified Au nanoplates and octahedral nanoparticles were determined by EDX spectra (Figures S8–S11). The contents of Ag and Au are 56.41 and 43.59 wt% for Au@Ag nanoplates (Figure S8) and 49.34 and 50.66 wt% for Au@Ag octahedral nanoparticles (Figure S10), respectively. The contents of Pd, Ag, and Au are 4.14, 22.1, and 73.76 wt% for AgPd nanodendrite-tipped Au nanoplates and 30.41, 21.41, and 48.19 wt% for AgPd nanodendrite-edge Au nanoplates, respectively (Figure S9). In addition, the contents of Pd, Ag, and Au are 11.47, 28.34, and 60.19 wt% for AgPd nanodendrite-tipped Au octahedral nanoparticles and 25.82, 31.01, and 43.17 wt% for AgPd nanodendrite-edged Au octahedral nanoparticles (Figure S11). These results indicate the successful site-selective growth of AgPd nanodendrites on different shapes of Au nanoparticles. This strategy thus serves as a general method for site-selective nanodendrite growth based on curvature-directed electron distribution, regardless of the shape of the central nanoparticles.

In addition to allowing site-selective growth of nanodendrites, this synthesis provides a simple, room-temperature method for preparation of noble metal catalysts. Other noble metal electrocatalysts, including AuCu,[24] carbon-supported PdPt,[70] and

19

Au@Pd core shell nanocatalysts,[71] have been prepared with the aid of thermal reduction, whereas the particles reported here were synthesized by galvanic replacement and co-reduction of Ag and Pd ions at room temperature. Moreover, previously reported noble metal electrocatalysts for CO2 reduction are primarily two-component systems, whereas the AgPd nanodendrite-modified Au nanoprisms reported in this work are unique, tri-component noble metal electrocatalysts where each component plays a role.

Electrochemical behavior of CO_2 at nanomaterial electrodes in aqueous solution. Nanomaterials described above were drop-cast onto a carbon rod for use as cathodes in an investigation of their efficiency for the electrochemical reduction of CO_2. Shown in Figure 4 are cyclic voltammograms recorded at carbon electrodes modified by deposition of prism, octahedral, and hexagonal nanomaterials composed of Au, Au@Ag core-shell, AgPd nanodendrite-tipped, and AgPd nanodendrite-edged Au in water containing 0.1 M $LiClO_4$ as supporting electrolyte. To simplify preparation and maintenance of the electrolyte solution, no buffer was used. Voltammograms were recorded at pH 4, which was reached upon saturation with CO_2. For all geometries, AgPd nanodendrite-edged Au nanoparticles show the least negative potential for CO_2 reduction; peak potentials are –0.18 V vs. RHE for prism and octahedral materials and –0.24 V vs. RHE for hexagonal nanoplates (Table 1). AgPd nanodendrite-tipped nanoparticles also display excellent catalytic activity, with reduction potentials of –0.27, –0.31, and –0.26 V vs. RHE for prism, octahedral, and hexagonal nanomaterials, respectively. Reduction of CO_2 at solid Au nanoparticles and Au@Ag core-shell

particles is less favorable, with reduction potentials ranging from –0.32 to –0.56 V vs.

RHE.

Controlled-potential electrolyses were used to determine product distributions

for the reduction of CO_2 at nanoprism-modified electrodes and to explore possible

reaction pathways. For electrolyses in water containing 0.1 M $LiClO_4$, headspace from

each electrolysis cell was analyzed by means of gas chromatography (GC) to detect

CO, and catholyte was analyzed by means of GC and NMR to determine solution-phase

products such as oxalic and formic acids. Bulk electrolyses were performed at peak

reduction potentials, determined by cyclic voltammetry, at which CO_2 reduction

proceeds with maximum efficiency compared to background processes. Electrolyses

yielded formate, which can be used in fuel cells,[72] at all nanoprism-modified electrodes.

No CO or other CO_2 reduction products were detected, indicating high selectivity for

production of formate. Faradaic efficiencies for CO_2 reduction to formate at Au,

Au@Ag, AgPd nanodendrite-tipped Au, and AgPd nanodendrite-edged Au nanoprisms

are 8%, 10%, 21%, and 49%, respectively, as calculated from total current passed and

known *n* values for CO_2 reduction reactions (Table 2).   Efficiency of formate

production increased considerably with Pd content, as AgPd nanodendrite-tipped Au

prisms (8.8 wt% Pd) and AgPd nanodendrite-edged Au prisms (25.5 wt% Pd) showed

a two-fold and five-fold increase, respectively, over pure Au and Au@Ag nanoprisms.

AgPd nanodendrite-edged prisms thus show both the most favorable reduction potential

and the highest faradaic efficiency for formate production in water.   Hydrogen

21

evolution is believed to be the primary competing reaction in all cases, as the formation

of bubbles at the electrode surface is observed during the course of an electrolysis.

The stability of AgPd nanodendrite-modified Au nanoprisms was investigated

by means repetitive bulk electrolyses, as well as TEM and SEM characterization. Up

to three consecutive electrolyses were performed at each electrode for a total

electrolysis time of 12 h, with no significant change in current density or product

formation between the first and third use. SEM and TEM images of nanoparticles were

compared before and after a 4-h electrolysis (Figure S12). The morphology of AgPd

nanodentrite-edged Au nanoprisms was largely unchanged, indicating that AgPd

nanodentrite-edged Au nanoprisms are highly stable during long-term electrolysis.

In Table 3, electrolysis results have been compared to a number of existing

reports of other electrode materials. Reduction potentials at AgPd nanodendrite-edged

nanoprisms, the most favorable potentials observed in this study, are considerably more

positive than most reported values and on par with branched Pd nanoparticles reported

by Klinkova and coworkers.[24,70,71,73-76] This improvement in reduction potential makes

AgPd nanodendrite-modified nanoprisms promising for scaled-up applications in

which applied potential and energy use are a concern. Current densities, calculated in

this work as an average current passed per geometric electrode area over the course of

electrolysis, are relatively low for AgPd nanodendrite-edged nanoprisms at only 0.2

mA/cm^2, relative to those of some other materials. Klinkova and coworkers have

reported current densities as high as 22 mA/cm^2 at branched Pd nanoparticles in water

containing 0.5 M $KHCO_3$, and other studies performed in bicarbonate electrolytes

22

report current densities in the range of 4–10 mA/cm^2.[70,73,74,77] However, the use of bicarbonate electrolytes in studies performed at pH 7 inflates the total availability if CO_2, leading to higher CO_2 concentrations at the electrode surface and thus increased currents.[78] This effect can be seen in a comparison of cyclic voltammetric currents at AgPd nanodendrite-tipped prisms in $LiClO_4$ and $NaHCO_3$ electrolytes (Figure S13), where current densities observed for CO_2 reduction in bicarbonate electrolyte are nearly 10 times higher than in the absence of bicarbonate at negative potentials. Bicarbonate is also known to be directly reduced by some metals, including Pd; Kanan and coworkers observed high current densities for formate production at Pd materials in bicarbonate buffer even in the absence of added CO_2.[79,80] In contrast, a recent study performed by Humphrey and coworkers with AuPd core-shell nanoparticles in unbuffered 0.1 M $NaSO_4$ achieved current densities similar to this work.[71] Similar trends are apparent in faradaic efficiencies reported at pH 7, which range from 10–97%, whereas efficiencies at pH 4 range from 27–49% (Table 3). Hydrogen evolution at pH 4 is believed to account for lowered faradaic efficiency compared to work performed at pH 7; in CV measurements, a small increase in current at pH 4 is seen compared to pH 7 at a similar reduction potential (Figure S14). Still, efficiency at AgPd nanodendrite-edged nanoprisms is high at 49% in comparison with materials investigated under similar conditions.

Electrochemical mechanisms for the reduction of CO_2 have been previously reported for a number of solvent–electrolyte systems.[81] Initially, adsorbed CO_2 or CO_2 in solution is reduced at the electrode surface to its corresponding radical anion, which

23

can then undergo further reaction along several established mechanistic pathways. For all electrode materials explored, electrolysis of CO_2 in unbuffered aqueous solvent leads primarily to the production of formate, which is generated when the CO_2 radical anion is protonated by water before accepting a second electron to afford formate (Scheme 2). This mechanism has been reported previously for the generation of formic acid or formate at Pd electrodes, and its relevance is believed to be greatest under acidic conditions.[81-84]

We propose that the unique structure and trimetallic composition of AgPd nanodendrite-modified Au nanoprisms could be responsible for the relatively positive reduction potential and high efficiency for CO_2 reduction (Scheme 3A). It has been reported that nanomaterials with more corner and edge sites show high catalytic activity for CO_2 reduction.[85,86] Au and Au@Ag core shell nanoprisms exhibit only a small number of these active sites due to their planar structure. In addition, Au surfaces are also capable of especially strong adsorption of carbon species, often resulting in poisoning of the catalyst surface;[86] prevalence of hydrogen evolution at the planar Au surface, a lack of sufficient corner and edge sites, and tight binding of CO_2 and its reduction products could explain the low yield of formate and poor catalytic activity on Au nanoprisms. Au@Ag nanoprisms suffer from similar limitations.

In contrast, the addition of AgPd nanodendrites to particle tips results in a dramatic increase in formate production and a considerably more favorable reduction potential. This is due in large part to an increase in active edge and corner sites at AgPd nanodendrites, which have high catalytic activity for CO_2 reduction.[85,86] In addition,

24

metal content and synergistic effects of Pd and Ag also play an important role. It has

been reported that short distances between active sites for surface stabilization of H^+

and CO_2 can aid in the formation of C–H bonds for formate production.[24] CO_2 can be

physically adsorbed on Au, Ag, and Pd metals, providing many possible sites for

adsorption of CO_2 on mixed-metal particles.[87] Although CO_2 can be adsorbed at Pd,

Pd is better known to have an affinity for hydrogen, resulting in high activity in

hydrogenation reactions as well as reversible adsorption and even incorporation of

hydrogen into Pd.[88,89] It is well established Pd will primarily adsorb hydrogen even in

the presence of CO_2.[90] Though similar studies have not been reported for Pd in

combination with Ag and Au, it is apparent from our cyclic voltammograms at pH 4 in

the presence and absence of CO_2 that a definite interaction with some form of hydrogen

occurs (S14). This would allow for optimized arrangement of both hydrogen and CO_2

on the particle surface and, concomitantly, a higher probability of their interaction at

the interface of the metals. Additionally, short distances between active sites for surface

stabilization of H^+ and CO_2 should result in easier formation of C–H bonds for formate

production (Scheme 3B).[24,87] When Pd content is increased to allow nanodendrite

formation over more of the particle surface, as is the case with AgPd nanodendrite-

edged Au nanoprisms, formate production and ease of reduction continue to improve,

indicating the higher catalytic activity of nanoparticles with more nanodendrites and

higher Pd content.

Although primary active sites for CO_2 reduction are presumed to be at the AgPd

nanodendrites, the Au core is also an important component of the nanoparticle. In

25

addition to its role in nanoparticle synthesis, immobilization of highly active nanodendrites on an Au core allows for optimized dispersion of their extensive edge and corner sites, high electrical conductivity, and high chemical stability over the course of electrolysis.[91] The resulting nanodendrite structure and synergistic effects of AgPd nanodendrite-modified Au nanoprisms leads to increased production of formate and more positive reduction potentials (Scheme 3A).

Electrocatalytic behavior of CO_2 at nanomaterial electrodes in an organic solvent. Electrocatalytic activities of the synthesized nanomaterials were also explored in acetonitrile containing 0.05 M $TMABF_4$, to take advantage of the greater solubility of CO_2 in organic solvents; CO_2 concentrations in acetonitrile have been reported as approximately 10 times higher than in aqueous solution.[92] Cyclic voltammograms for reduction of CO_2 at each electrode are shown in Figure 5, and a summary of peak potentials is included in Table 1. Electrodes prepared with AgPd nanodendrite-tipped and -edged Au nanomaterials of different geometries all show similar behavior. In each case, a single cathodic peak is present between –1.58 and –1.69 V vs. SHE. Cyclic voltammograms at Au and Au@Ag core-shell nanomaterials show multiple peaks, indicating different reaction pathways and products formed upon reduction of CO_2. Au nanomaterials exhibit one peak between –1.32 and –1.39 V vs. SHE, with a second peak between –1.58 and –1.98 V vs. SHE. The potential of the more negative peak is greatly dependent on particle geometry. Au@Ag core-shell nanomaterials show similar behavior, though the first reduction peak is more negative than that for Au (–1.47 to –1.51 V vs. SHE).

26

Controlled-potential (bulk) electrolyses were used to determine the products of CO_2 reduction. Gas chromatographic analysis of solution headspace and catholyte treated with BSTFA:TCMS was used to detect all products except formate. Solution-phase products were quantitated by comparison to an internal standard, whereas quantitation of CO was achieved with a calibration curve (Figure S15). The presence of formate was probed with NMR, and not detected for electrolyses in organic solvents. Table 4 shows faradaic efficiencies for the formation of a range of products resulting from electrolysis in acetonitrile containing TMABF4, including CO (used as fuel for solid oxide fuel cells as well as syngas),[93] oxalic acid, and further reduction products of oxalic acid. AgPd nanodendrite-tipped and -edged Au prisms show remarkable efficiency for the production of CO gas, at 87 and 85%, respectively, after electrolysis at –1.5 V vs. SHE. No other products were detected from electrolyses at these electrodes, indicating high product selectivity. Electrolyses at Au and Au@Ag core-shell prisms were performed at both –1.5 and –1.9 V vs. SHE to explore the products generated at both peaks observed for cyclic voltammograms. At –1.5 V vs. SHE (the same potential used for electrolysis at AgPd nanodendrite electrodes), Au and Au@Ag core-shell nanoprisms show a faradaic efficiency for CO production of only 64% and 54%, respectively. The remaining current leads to the formation of oxalic acid, which is then immediately reduced to glyoxylic and glycolic acid. Efficiency of CO production was lower at –1.9 V vs. SHE, at only 45% for Au prisms and 43% for Au@Ag core-shell prisms. The remaining products are again oxalic, glyoxylic, and glycolic acid. Additionally, trends in faradaic efficiencies indicate that the less negative

27

CO_2 reduction peak seen at Au and Au@Ag core-shell prisms is likely due to formation

of CO; however, even electrolyses at this potential generate a mixture of products.

These results indicate that AgPd nanodendrite-modified Au prisms are more selective

for production of CO than prisms without Pd.

In an organic solvent, CO_2 reduction appears to follow a different set of reaction

pathways than observed in aqueous conditions (Scheme 4). CO_2 is reduced at the

electrode surface to its corresponding radical anion, as is the case in an aqueous

mechanism. CO_2 radical anions can then form an intermediate adduct with an

unreduced CO_2 molecule through coupling of carbon and oxygen before accepting a

second electron, resulting in the cleavage of a C–O bond to form CO gas and a

carbonate ion.[82] A CO_2 radical anion may also undergo radical coupling with a second

radical anion to form oxalate, which can then be protonated by adventitious water to

form oxalic acid.[82] Oxalic acid is capable of undergoing a two-electron reduction in

the presence of H^+ to form glyoxylate, followed by subsequent two-electron reduction

to afford glycolate.[94]

To understand better the mechanism by which oxalic acid and its reduction

products are formed at Au and Au@Ag core-shell nanoprisms, additional cyclic

voltammograms were recorded at Au@Ag core-shell nanoprisms in the presence and

absence of known quantities of water (Figure S15). The more negative cyclic

voltammetric peaks observed at Au@Ag core-shell prisms increase in current with the

addition of water, indicating an expected dependence on H^+. The absence of a second

voltammetric peak at AgPd nanodendrite Au electrodes and the lack of oxalic acid and

28

its reduction products after electrolysis indicate that Pd content suppresses the CO_2 radical anion coupling reaction.

As CO is the dominant reaction product observed, Table 5 compares results obtained here with other reports in the literature for the formation of CO at various nanomaterials.[22-24,73,85,95] All potentials from the literature are reported in V vs. SHE for ease of comparison. Although the reduction potential of CO_2 at AgPd-edged Au nanoprisms is considerably more negative in acetonitrile than in water, and indeed more negative than the potential required to produce CO at other materials in water, the faradaic efficiency for CO production is moderately high. Current densities of 2 mA cm^{-2} are lower than others reported, but ten times higher than those obtained in water at the same materials. This corresponds to the difference in CO_2 solubility between solvents. Additionally, although negative reduction potentials and low current densities may not make these particles immediately competitive with other state-of-the-art materials for CO formation, the ability to control product distributions by tuning of the solvent-electrolyte system and particle composition is of great interest and lays groundwork for further optimization.

Roles of Au, Ag, and Pd in altering the distribution of CO_2 reduction products are not known with certainty, but existing literature lends itself to a discussion of possible synergistic effects. First, formation of oxalate, which appears to compete with CO formation, requires the distance between CO_2 radical anions to be small enough for radical coupling to occur (Scheme 5A). Carbon species can be strongly adsorbed at both Au and Ag surfaces, allowing for a relatively high density of adsorbed CO_2 radical

29

anions at Au and Ag@Au core shell nanoprisms.[87] This encourages coupling of the adsorbed species. Once formed, oxalate is then immediately reduced in wet solvent.

In the case of AgPd nanodendrite-modified Au nanoprisms, oxalate is no longer formed and CO is the only product detected. Though Ag and Pd are both capable of adsorbing CO_2, Pd has been shown to favor hydrogen;[90] even at low concentrations, adventitious water can have a large effect on electrochemical behavior and may allow adsorbed hydrogen at Pd active sites. This would increase the distance between adsorbed CO_2 radical anions, preventing radical coupling (Scheme 5B). Although it is possible that oxalate or similar coupling products may still form on the Au core of the particle, no such products were detected, reinforcing the conclusion that the primary active sites for CO_2 reduction on AgPd nanodendrite-modified Au nanoprisms are the edge and corner sites present on the nanodendrite structure.[85,86]

Conclusions

A facile method for site-selective growth of AgPd nanodendrites on Au nanoparticles is reported that combines the galvanic replacement of Ag layers on Au@Ag nanoprisms with H_2PdCl_4 and a co-reduction process of silver and palladium ions. Selective deposition of the AgPd nanodendrites on tips or edges of Au nanoprisms can be controlled by variation of the concentration of H_2PdCl_4. This site-selective growth approach is universally applicable to other central nanoparticles of various shapes. More importantly, these AgPd nanodendrite-modified Au nanoprisms show high electrochemical activity for CO_2 reduction. In aqueous electrolyte, the AgPd

30

nanodendrite-edged Au nanoprisms show the most favorable reduction potential for CO_2, at –0.18 V vs. RHE, compared to previously reported nanocatalysts. They also show higher faradaic efficiencies than Au, Au@Ag, and AgPd nanodendrite-tipped Au nanoprisms. In $TMABF_4$–ACN electrolyte, higher faradaic efficiencies and selectivity for CO reduction products were obtained with AgPd nanodendrite-modified Au nanoprisms compared to Au and Au@Ag nanoprisms. The high electrocatalytic ability of AgPd nanodendrite-modified Au nanoprisms is attributed to their unique structures and synergistic effects among Ag, Pd and Au. Moreover, AgPd nanodendrite-modified Au nanoprisms show excellent stability during long electrolysis and can be used repetitively with no significant change in performance. These transformative results indicate the potential application of AgPd modified Au materials in the conversion of CO_2 into useful fuels.

Acknowledgments

Supporting Information

31

Details on nanomaterial structure and contents (Figures S1–11), particle stability (Figure S12), and additional electrochemical experiments (Figures S13-S15) are provided.
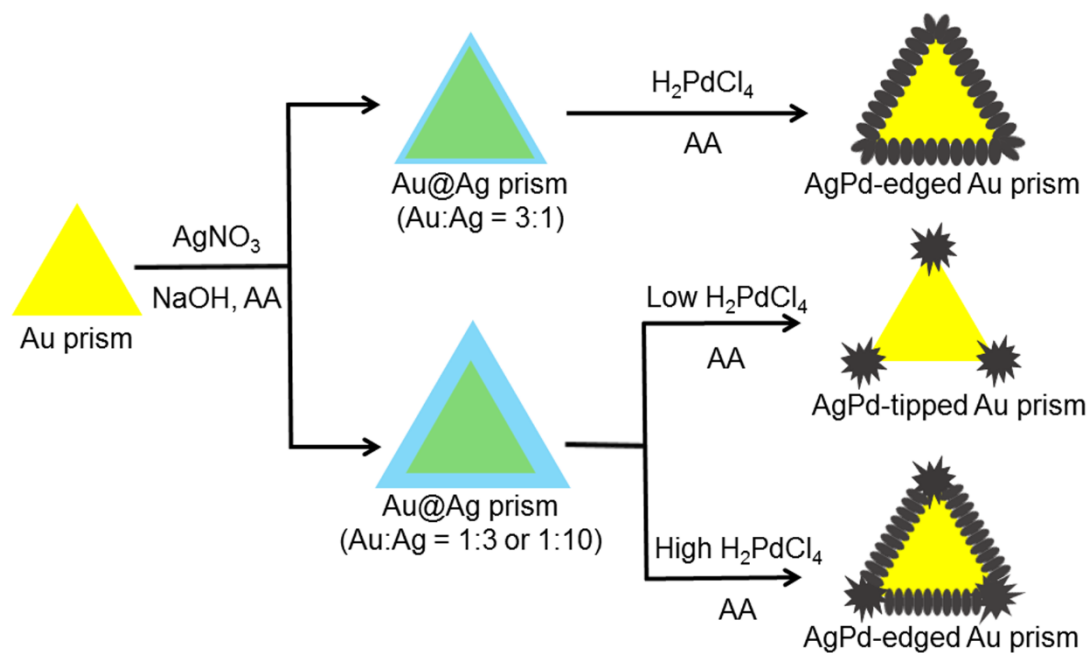
Scheme 1

Scheme 1. Synthetic approach to the preparation of AgPd nanodendrite-tipped and -

edged Au nanoprisms.

Figure 1
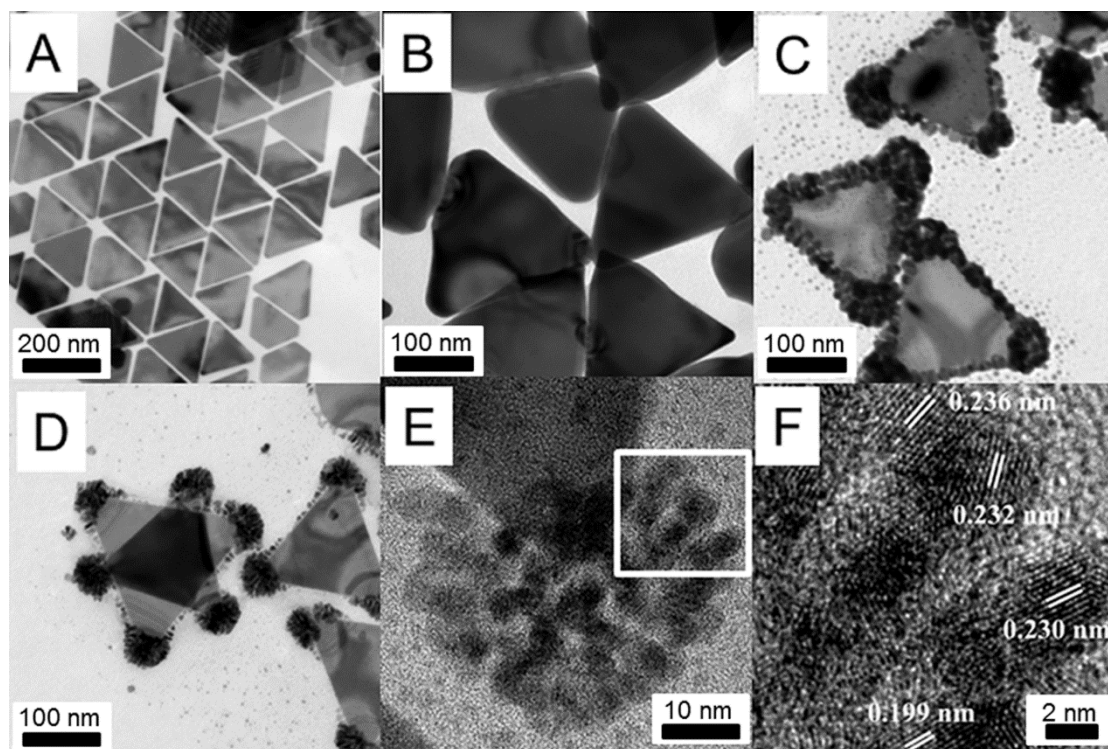
Figure 1. TEM images of synthetic Au nanoprisms (A), Au@Ag core-shell nanoprisms (B), AgPd nanodendrite-edged nanoprisms (C), and AgPd nanodendrite-tipped Au nanoprisms (D). HRTEM image of AgPd nanodendrite-tipped Au nanoprisms (E) and enlarged image of the selected region (F).

34
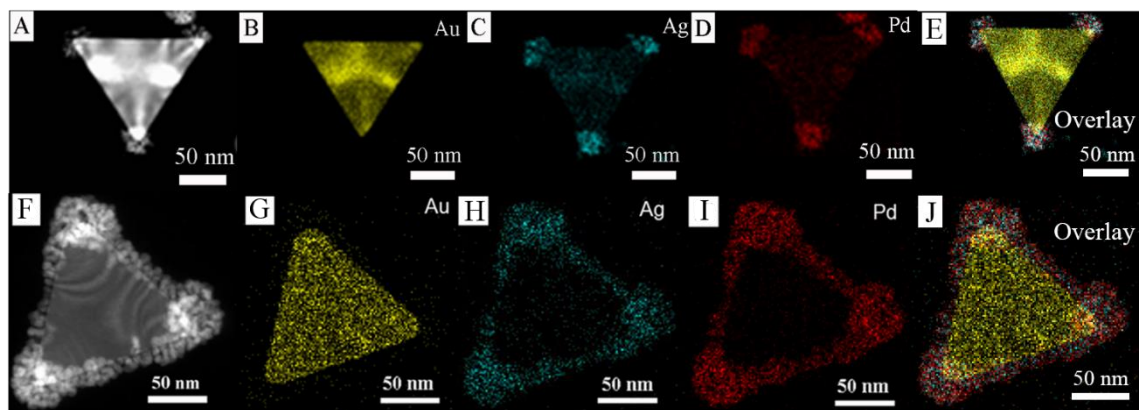
Figure 2

Figure 2. STEM image of a AgPd nanodendrite-tipped Au nanoprism (A) and corresponding EDX elemental mapping images of Au (B), Ag (C), Pd (D) and overlay (E). A similar STEM image of a AgPd nanodendrite-edged Au nanoprism (F) is shown with EDX elemental mapping images of Au (G), Ag (H), Pd (I) and overlay (J).

35
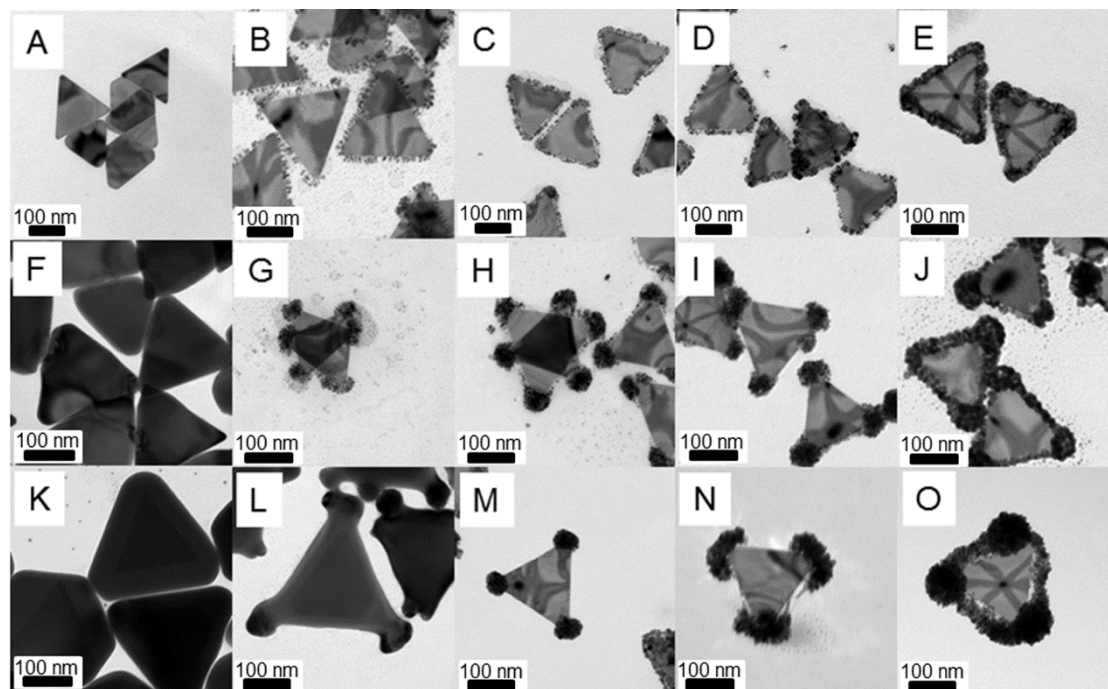
Figure 3

Figure 3. TEM images of AgPd nanodendrite-modified Au nanoprisms with different amounts of Ag coating and H_2PdCl_4. On the far left, (A), (F), and (K) show TEM images of Au@Ag core-shell nanoprisms with Au:Ag ratios of 3:1, 1:3, and 1:10, respectively. Prisms shown in (A) were treated with different amounts of H_2PdCl_4 to produce nanodendrite-tipped and -edged prisms shown in frames (B)–(E) as follows: 10 µL of 2 mM H_2PdCl_4 (B), 20 µL of 2 mM H_2PdCl_4 (C), 10 µL of 10 mM H_2PdCl_4 (D), and 40 µL of 10 mM H_2PdCl_4 (E). Similarly, prisms shown in (F) and (K) were treated with the same amounts of H_2PdCl_4 to produce prisms in frames (G)–(J) and (L)–(O), respectively.

Figure 4
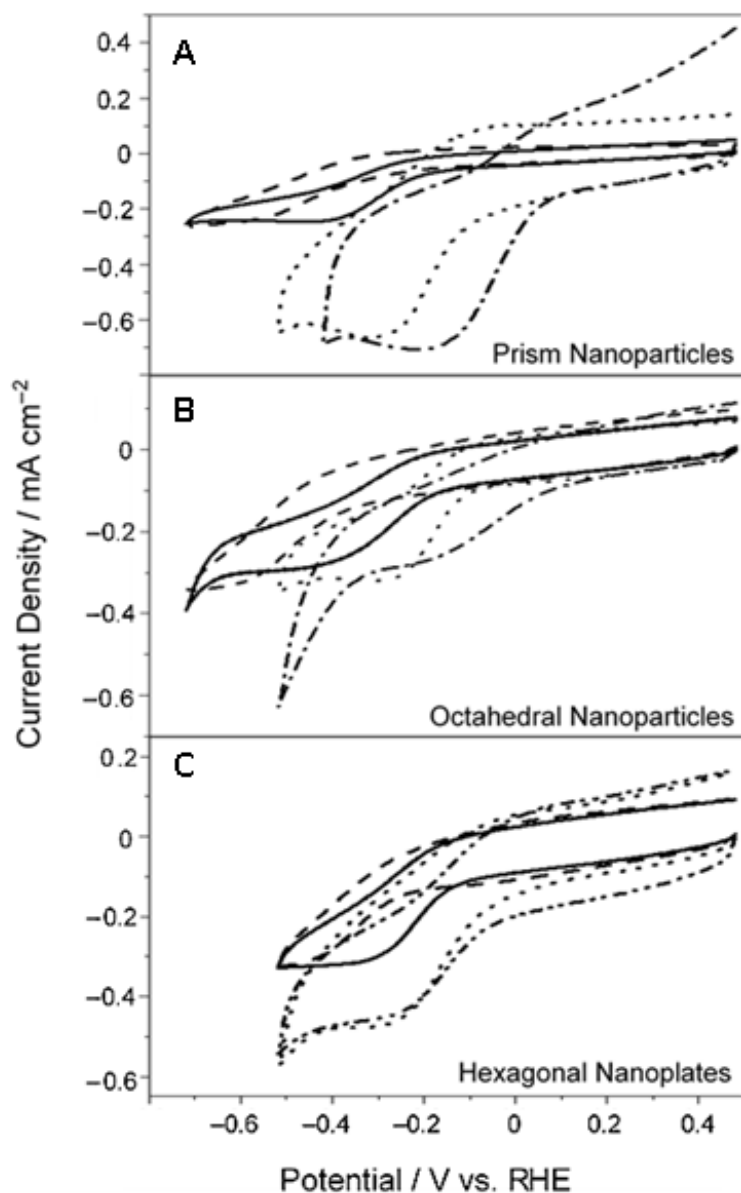
Figure 4. Cyclic voltammograms recorded at 100 mV s^{-1} for the reduction of a solution

saturated with CO_2 in oxygen-free water containing 0.1 M $LiClO_4$ at pH 4. Glassy

carbon cathodes (area = 0.071 cm^2) were modified with prism (A), octahedral (B), and

hexagonal (C) nanomaterials composed of Au (solid line), Au@Ag (dashed line), AgPd

nanodendrite-tipped Au (dotted line), or AgPd nanodendrite-edged Au (dash-dot line).

37

Table 1. Peak potentials of nanomaterials with different geometry and metal content in either water containing 0.10 M LiClO$_4$ or in ACN containing 0.05 M TMABF$_4$. Potentials are reported with respect to a reversible hydrogen electrode (RHE) in the aqueous medium and a standard hydrogen electrode (SHE) in the organic solvent.

Water (V vs. RHE)				
	1	**2**	**3**	**4**
Prism	–0.42	–0.53	–0.27	–0.18
Octahedron	–0.37	–0.56	–0.31	–0.18
Hexagonal Plate	–0.31	–0.47	–0.26	–0.24

Acetonitrile (V vs. SHE)				
	1	**2**	**3**	**4**
Prism	–1.39, –1.95	–1.51, –1.88	-1.69	-1.66
Octahedron	–1.32, –1.82	–1.47	-1.58	-1.63
Hexagonal Plate	–0.38, –1.58	–1.51, –1.77	-1.62	-1.69

1 = Au; **2** = Au@Ag core-shell; **3** = AgPd nanodendrite-tipped Au; **4** = AgPd nanodendrite-edged Au

38

Table 2. Faradaic efficiencies for products arising from controlled-potential electrolyses of CO_2 at various nanoprism electrodes in water–0.10 M $LiClO_4$. Potentials referenced to RHE.

Prism Material	E (V)	Faradaic Efficiency (%)[a] HCOOH[b]
1	–0.42	8
2	–0.52	10
3	–0.27	21
4	–0.18	49

1 = Au; **2** = Au@Ag core-shell; **3** = AgPd nanodendrite-tipped Au;

4 = AgPd nanodendrite-edged Au

[a] Faradaic efficiency expressed as the percent of measured current attributed to a given process.

[b] HCOOH identified and quantitated by means of NMR measurements with an internal standard.

39

Table 3. Comparison of materials used for reduction of CO_2 to formate/formic acid.

All potentials are reported with respect to the reversible hydrogen electrode (RHE).

Catalyst	E (V)	Electrolyte	Faradaic Efficiency	Ref.
3D porous hollow fiber Cu	–0.40	0.3 M $KHCO_3$ (pH 7)*	10%	73
SnO_2 porous nanowires	–0.80	0.1 M $KHCO_3$ (pH 6.8)*	78%	76
Cu-CDots nanocorals	–0.70	0.5 M $KHCO_3$ (pH 7.2)	68%	77
C-supported Pd–Pt NPs	–0.40	0.1 M KH_2PO_4/0.1 M K_2HPO_4 (pH 6.7)	88%	70
Branched Pd NPs	–0.20	0.5 M $KHCO_3$ (pH 7.2)	97%	74
Tin	–1.30	0.1 M Na_2SO_4 (pH 4)	40%	75
Au-Pd core-shell NPs	–0.50	Na_2SO_4 (pH 4)	27%	71
AgPd-edged Au nanoprisms	–0.18	0.1 M $LiClO_4$ (pH 4)	49%	This work

*Not provided in text; determined in this work.

Scheme 2

(1) $CO_2 + e^- \longrightarrow CO_2^{-\bullet}$

(2) $CO_2^{-\bullet} + H^+ + e^- \longrightarrow HCOO^-$
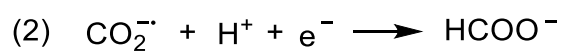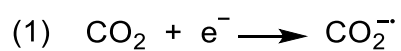
Scheme 2. Proposed mechanism for the reduction of CO_2 to formic acid in aqueous

electrolyte.

41

1
2
3
4
5
6
7
8
9
10
11
12
13
14
15
16
17
18
19
20
21
22
23
24
25
26
27
28
29
30
31
32
33
34
35
36
37
38
39
40
41
42
43
44
45
46
47
48
49
50
51
52
53
54
55
56
57
58
59
60
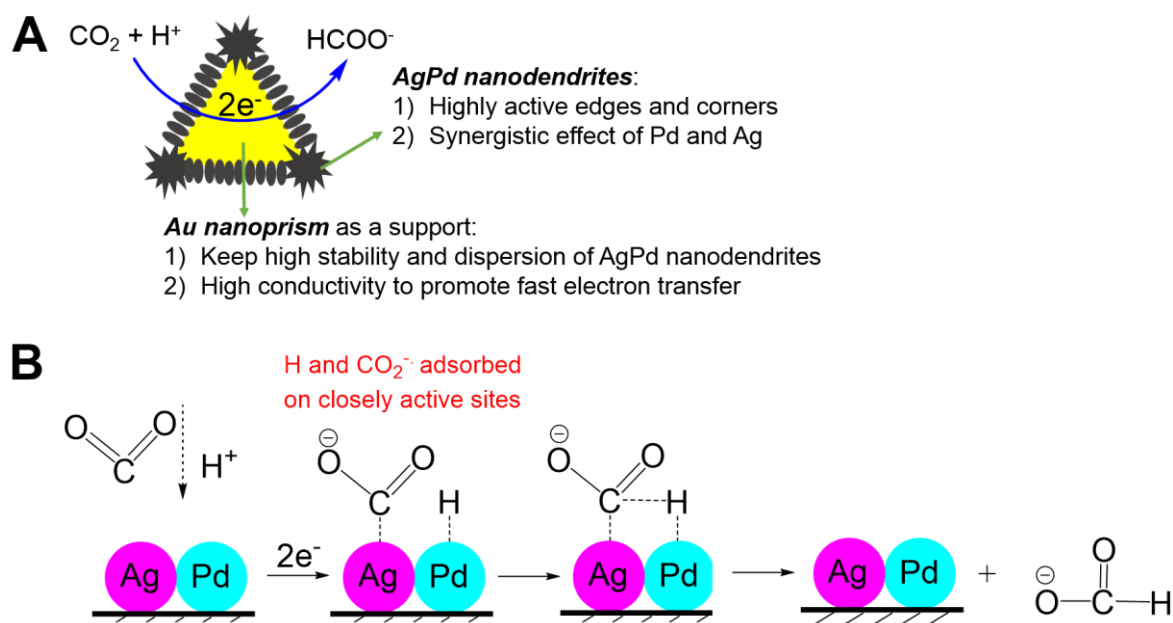
Scheme 3.

Scheme 3. (A) Electrocatalytic mechanism of CO_2 reduction on AgPd nanodendrite-modified Au nanoprisms; (B) Proposed synergistic effect of AgPd nanodendrites.[87–90]

Figure 5.
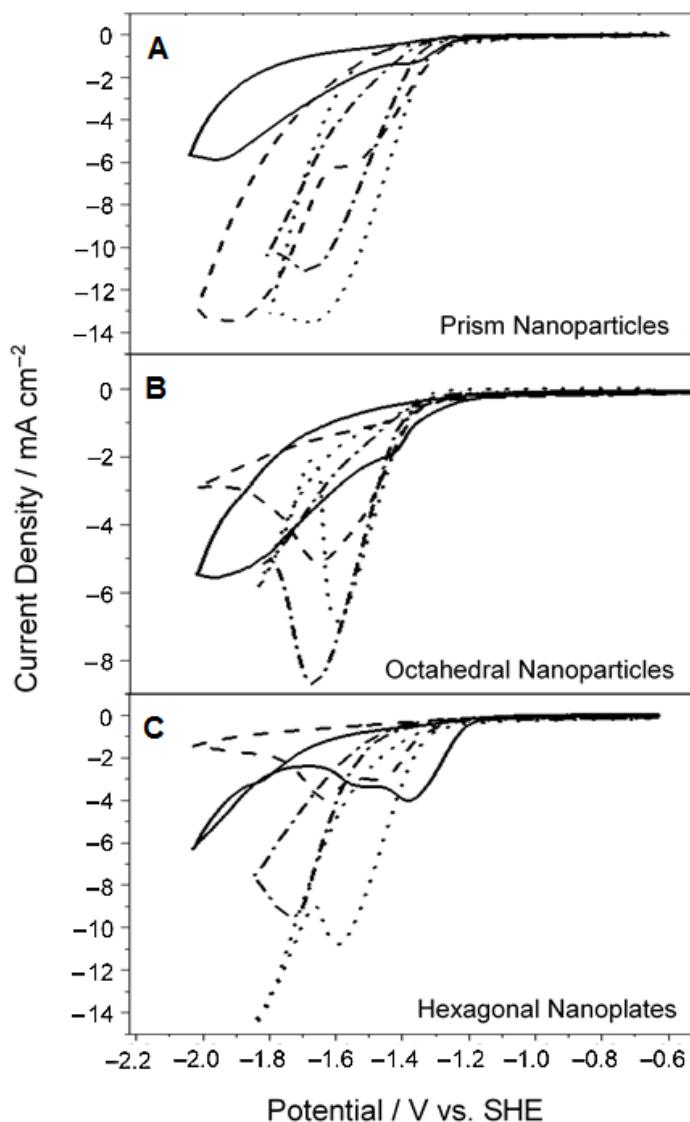
Figure 5. Cyclic voltammograms recorded at 100 mV s^{-1} for the reduction of a solution

saturated with CO_2 in oxygen-free ACN containing 0.05 M TMABF$_4$. Glassy carbon

cathodes (area = 0.071 cm^2) were modified with prism (A), octahedral (B), and

hexagonal (C) nanomaterials composed of Au (solid line), Au@Ag core-shell (dashed

line), AgPd nanodendrite-edged Au (dash-dot line) or AgPd nanodendrite-tipped Au

(dotted line).

43

Table 4. Faradaic efficiencies for products arising from controlled-potential electrolyses of CO_2 at various nanoprism electrodes in ACN–0.050 M $TMABF_4$. Potentials reported as V vs. SHE.

Prism Material	E (V)	Faradaic Efficiency (%)[a]				
		CO[b]	Oxalic Acid[c]	Glycolic Acid[c]	Glyoxylic Acid[c]	Total
1	–1.52	64	8	13	TR	85
1	–1.92	45	12	27	TR	84
2	–1.52	54	14	26	TR	94
2	–1.92	43	24	13	TR	80
3	–1.52	87	–	–	–	87
4	–1.52	85	–	–	–	85

1 = Au; **2** = Au@Ag core-shell; **3** = AgPd nanodendrite-tipped Au; **4** = AgPd nanodendrite-edged Au.

[a] Faradaic efficiency expressed as percent of measured current attributable to a given process.

[b] CO was identified and quantitated by means of gas chromatography with a TCD and a standard calibration curve.

[c] Oxalic, glyoxylic, and glycolic acids were derivatized to the corresponding trimethylsilyl esters and detected by means of gas chromatography with *n*-hexadecane as an internal standard.

[d] TR = trace.

Scheme 4

(1) $CO_2 + e^- \longrightarrow CO_2^{-\bullet}$

(2) $CO_2^{-\bullet} + CO_2 \longrightarrow$ [structure]	
(3) [structure] $+ e^- \longrightarrow CO + CO_3^{2-}$	Primary reactions at AgPd nanodendrite-tipped and -edged Au materials
(4) $CO_2^{-\bullet} + CO_2^{-\bullet} \longrightarrow$ [structure]	
(5) [structure] $+ 2\,H_2O + 2\,e^- \longrightarrow$ [structure] $+ 3\,OH^-$	Competing reactions at Au and Au@Ag materials
(6) [structure] $+ 2\,H_2O + 2\,e^- \longrightarrow$ [structure] $+ 2\,OH^-$	
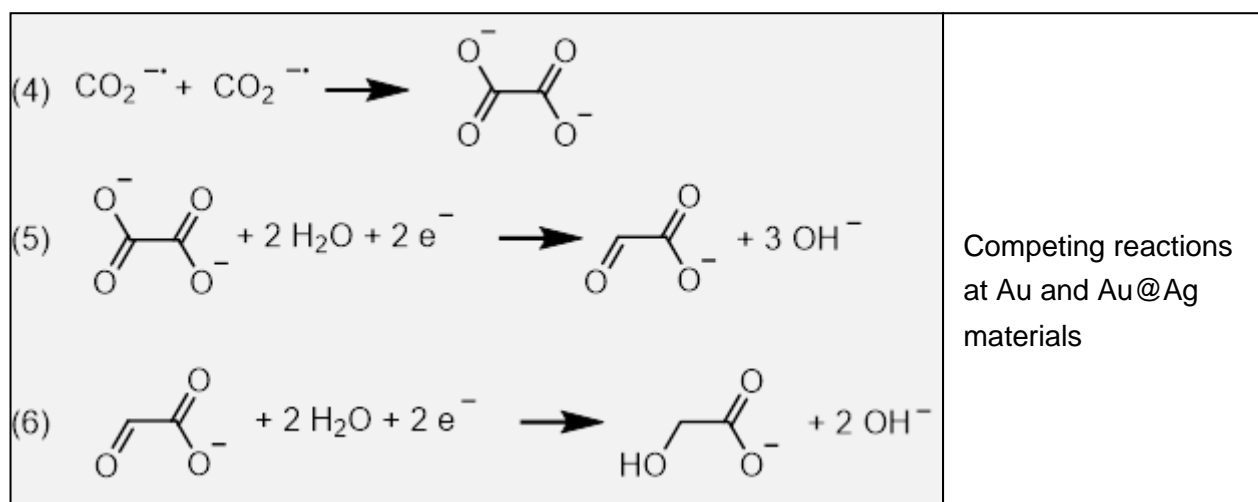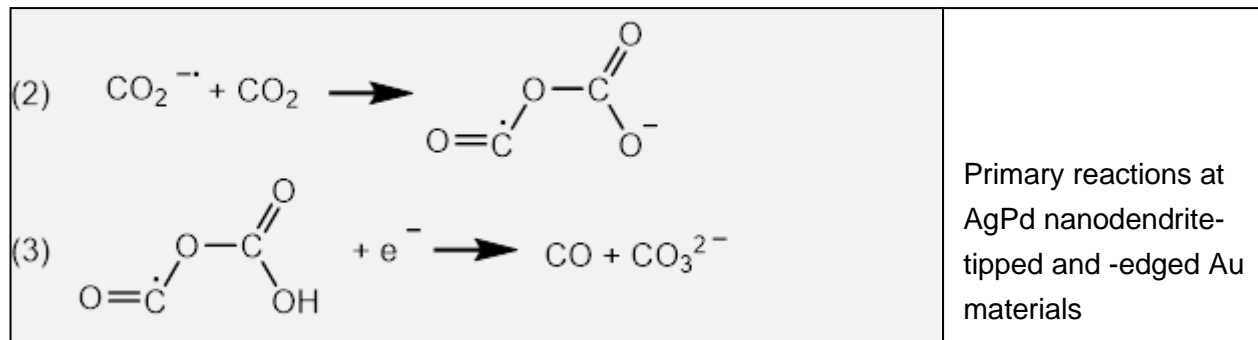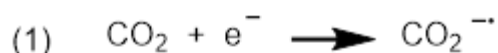
Scheme 4. Proposed mechanisms for reduction of CO_2 to CO, oxalate, glyoxylate, and

glycolate in organic solvent–electrolyte.

45

Table 5. Comparison of materials used for reduction of CO_2 to CO. All potentials are reported with respect to the standard hydrogen electrode (SHE).

Catalyst	E (V)	Electrolyte	Faradaic Efficiency	Ref.
7.7 nm Au NPs	−1.60	0.1 M $KHCO_3$ (pH 6.8)	45%	85
3.7 nm Pd NPs	−1.29	0.1 M $KHCO_3$ (pH 6.8)	91.2%	23
Nanoporous Ag	−1.02	0.5 M $KHCO_3$ (pH 7.2)	92%	22
Au_3Cu bimetallic NPs	−1.13	0.1 M $KHCO_3$ (pH 6.8)	63%	24
3D porous hollow fiber Cu	−0.40	0.3 M $KHCO_3$ (pH 7)*	75%	73
WSe_2 nanoflakes	−0.95	$EMIM-BF_4:H_2O$ (pH 3.2)	90%	96
Nb-doped MoS_2	−1.00	$EMIM-BF_4:H_2O$ (pH 3.2)	82%	97
AgPd-edged Au nanoprisms	−1.66	0.05 M $TMABF_4$ (in ACN)	85%	This work

*Not provided in text; determined in this work

Note: Since pH measurements in an organic solvent are impractical, and use of the RHE reference potential thus difficult, all potentials from the literature have been converted to V vs. SHE for ease of comparison.

46
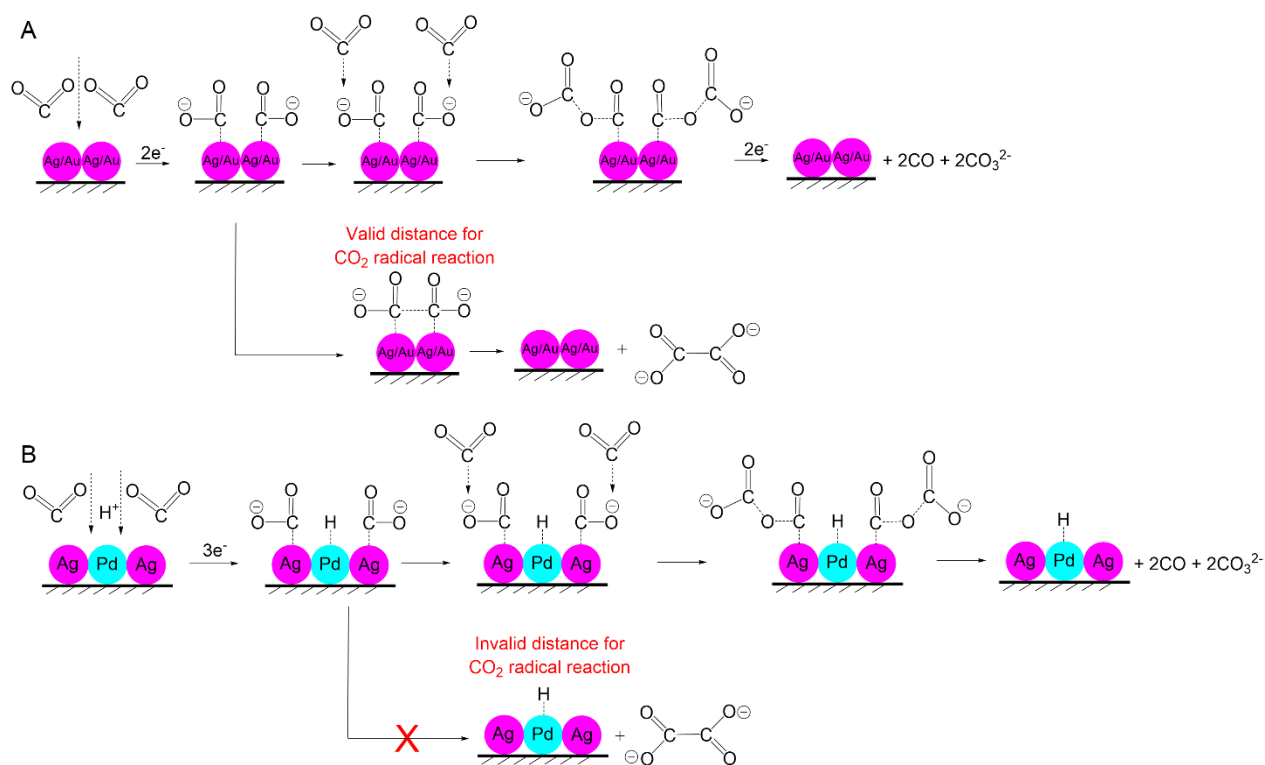
Scheme 5

Scheme 5. (A) CO_2 reduction mechanism at Au and Au@Ag core shell nanoprisms for

CO and oxalate; (B) CO_2 reduction mechanism at AgPd nanodendrite-modified Au

nanoprisms for CO as the only product.

References

(1)   Dresselhaus, M. S.; Thomas, I. L. Alternative energy technologies. *Nature* **2001,** *414*, 332–337.

(2)   Lewis, N. S.; Nocera, D. G. Powering the planet: Chemical challenges in solar energy utilization. *P. Natl. Acad. Sci. USA* **2006,** *103*, 15729–15735.

(3)   Yang, P.; Tarascon, J.-M. Towards systems materials engineering. *Nat. Mater.* **2012,** *11*, 560–563.

(4)   D'Alessandro, D. M.; Smit, B.; Long, J. R. Carbon Dioxide Capture: Prospects for New Materials. *Angew. Chem. Int. Ed.* **2010,** *49*, 6058–6082.

(5)   Goeppert, A.; Czaun, M.; May, R. B.; Prakash, G. K. S.; Olah, G. A.; Narayanan, S. R. Carbon Dioxide Capture from the Air Using a Polyamine Based Regenerable Solid Adsorbent. *J. Am. Chem. Soc.* **2011,** *133*, 20164–2167.

(6)   Savéant, J. M.; Tard, C. Attempts To Catalyze the Electrochemical CO2-to-Methanol Conversion by Biomimetic 2e(-)+2H(+) Transferring Molecules. *J. Am. Chem. Soc.* **2016,** *138*, 1017–1021.

(7)   Centi, G.; Perathoner, S. Opportunities and prospects in the chemical recycling of carbon dioxide to fuels. *Catal. Today* **2009,** *148*, 191–205.

(8)   Akhter, P.; Farkondehfal, M. A.; Hernandez, S.; Hussain, M.; Fina, A.; Saracco, G.; Khan, A. U.; Russo, N. Environmental issues regarding CO2 and recent strategies for alternative fuels through photocatalytic reduction with titania-based materials. *J. Environ. Chem. Eng.* **2016,** *4*, 3934–3953.

(9)   Guo, Z. G.; Cheng, S. W.; Cometto, C.; Arncolabehere-Mallart, E.; Ng, S. M.; Ko, C. C.; Liu, G. J.; Chen, L. J.; Robert, M.; Lau, T. C. Highly Efficient and Selective Photocatalytic CO2 Reduction by Iron and Cobalt Quaterpyridine Complexes. *J. Am. Chem. Soc.* **2016,** *138*, 9413–9416.

(10)   Qiao, J.; Liu, Y.; Hong, F.; Zhang, J. A review of catalysts for the electroreduction of carbon dioxide to produce low-carbon fuels. *Chem. Soc. Rev.* **2014,** *43*, 631–675.

(11)   Li, C. W.; Kanan, M. W. CO_2 Reduction at Low Overpotential on Cu Electrodes Resulting from the Reduction of Thick Cu_2O Films. *J. Am. Chem. Soc.* **2012,** *134*, 7231–7234.

(12)   Machan, C. W.; Yin, J.; Chabolla, S. A.; Gilson, M. K.; Kubiak, C. P. Improving the Efficiency and Activity of Electrocatalysts for the Reduction of CO_2 through Supramolecular Assembly with Amino Acid-Modified Ligands. *J. Am. Chem. Soc.* **2016,** *138*, 8184–8193.

(13)   Medina-Ramos, J.; Pupillo, R. C.; Keane, T. P.; DiMeglio, J. L.; Rosenthal, J. Efficient Conversion of CO_2 to CO Using Tin and Other Inexpensive and Easily Prepared Post-Transition Metal Catalysts. *J. Am. Chem. Soc.* **2015,** *137*, 5021–5027.

(14)   Jhong, H.-R. M.; Ma, S.; Kenis, P. J. A. Electrochemical conversion of CO_2 to useful chemicals: current status, remaining challenges, and future opportunities. *Curr. Opin. Chem. Eng.* **2013,** *2*, 191–199.

(15)   Zhu, W.; Michalsky, R.; Metin, O.; Lv, H.; Guo, S.; Wright, C. J.; Sun, X.; Peterson, A. A.; Sun, S. Monodisperse Au Nanoparticles for Selective Electrocatalytic Reduction of CO_2 to CO. *J. Am. Chem. Soc.* **2013,** *135*, 16833–16836.

48

(16) Rosen, B. A.; Salehi-Khojin, A.; Thorson, M. R.; Zhu, W.; Whipple, D. T.; Kenis, P. J. A.; Masel, R. I. Ionic Liquid-Mediated Selective Conversion of CO_2 to CO at Low Overpotentials. *Science* **2011,** *334*, 643–644.

(17) Kumar, B.; Asadi, M.; Pisasale, D.; Sinha-Ray, S.; Rosen, B. A.; Haasch, R.; Abiade, J.; Yarin, A. L.; Salehi-Khojin, A. Renewable and metal-free carbon nanofibre catalysts for carbon dioxide reduction. *Nat. Commun.* **2013,** *4:2819*.

(18) Zhang, S.; Kang, P.; Meyer, T. J. Nanostructured Tin Catalysts for Selective Electrochemical Reduction of Carbon Dioxide to Formate. *J. Am. Chem. Soc.* **2014,** *136*, 1734–1737.

(19) Cao, Z.; Kim, D.; Hong, D. C.; Yu, Y.; Xu, J.; Lin, S.; Wen, X. D.; Nichols, E. M.; Jeong, K.; Reimer, J. A.et al. A Molecular Surface Functionalization Approach to Tuning Nanoparticle Electrocatalysts for Carbon Dioxide Reduction. *J. Am. Chem. Soc.* **2016,** *138*, 8120–8125.

(20) Chen, Y.; Li, C. W.; Kanan, M. W. Aqueous CO2 Reduction at Very Low Overpotential on Oxide-Derived Au Nanoparticles. *J. Am. Chem. Soc.* **2012,** *134*, 19969–19972.

(21) Salehi-Khojin, A.; Jhong, H.-R. M.; Rosen, B. A.; Zhu, W.; Ma, S.; Kenis, P. J. A.; Masel, R. I. Nanoparticle Silver Catalysts That Show Enhanced Activity for Carbon Dioxide Electrolysis. *J. Phy. Chem. C* **2013,** *117*, 1627–1632.

(22) Lu, Q.; Rosen, J.; Zhou, Y.; Hutchings, G. S.; Kimmel, Y. C.; Chen, J. G.; Jiao, F. A selective and efficient electrocatalyst for carbon dioxide reduction. *Nat. Commun.* **2014,** *5: 324*.

(23) Gao, D.; Zhou, H.; Wang, J.; Miao, S.; Yang, F.; Wang, G.; Wang, J.; Bao, X. Size-Dependent Electrocatalytic Reduction of CO2 over Pd Nanoparticles. *J. Am. Chem. Soc.* **2015,** *137*, 4288–4291.

(24) Kim, D.; Resasco, J.; Yu, Y.; Asiri, A. M.; Yang, P. Synergistic geometric and electronic effects for electrochemical reduction of carbon dioxide using gold-copper bimetallic nanoparticles. *Nat. Commun.* **2014,** *5: 4948*.

(25) Lim, B.; Xia, Y. N. Metal Nanocrystals with Highly Branched Morphologies. *Angew. Chem. Int. Ed.* **2011,** *50*, 76–85.

(26) Motl, N. E.; Smith, A. F.; DeSantis, C. J.; Skrabalak, S. E. Engineering plasmonic metal colloids through composition and structural design. *Chem. Soc. Rev.* **2014,** *43*, 3823–3834.

(27) Yu, Y.; Zhang, Q. B.; Xie, J. P.; Lee, J. Y. Engineering the architectural diversity of heterogeneous metallic nanocrystals. *Nat. Commun.* **2013,** *4: 1454*.

(28) DeSantis, C. J.; Peverly, A. A.; Peters, D. G.; Skrabalak, S. E. Octopods versus Concave Nanocrystals: Control of Morphology by Manipulating the Kinetics of Seeded Growth via Co-Reduction. *Nano Lett.* **2011,** *11*, 2164–2168.

(29) Zhu, J.; Zhang, F.; Li, J.-J.; Zhao, J.-W. The effect of nonhomogeneous silver coating on the plasmonic absorption of Au-Ag core-shell nanorod. *Gold Bull.* **2014,** *47*, 47–55.

(30) Yoo, H.; Millstone, J. E.; Li, S.; Jang, J.-W.; Wei, W.; Wu, J.; Schatz, G. C.; Mirkin, C. A. Core-Shell Triangular Bifrustums. *Nano Lett.* **2009,** *9*, 3038–3041.

(31) Tsao, Y.-C.; Rej, S.; Chiu, C.-Y.; Huang, M. H. Aqueous Phase Synthesis of Au-Ag Core-Shell Nanocrystals with Tunable Shapes and Their Optical and Catalytic Properties. *J. Am. Chem. Soc.* **2014,** *136*, 396–404.

49

(32) Lu, C.-L.; Prasad, K. S.; Wu, H.-L.; Ho, J.-a. A.; Huang, M. H. Au Nanocube-Directed Fabrication of Au-Pd Core-Shell Nanocrystals with Tetrahexahedral, Concave Octahedral, and Octahedral Structures and Their Electrocatalytic Activity. *J. Am. Chem. Soc.* **2010,** *132*, 14546–14553.

(33) Weiner, R. G.; Skrabalak, S. E. Metal Dendrimers: Synthesis of Hierarchically Stellated Nanocrystals by Sequential Seed-Directed Overgrowth. *Angew. Chem. Int. Ed.* **2015,** *54*, 1181–1184.

(34) Zhou, L.; Liu, Z.; Zhang, H.; Cheng, S.; Fan, L.-J.; Ma, W. Site-specific growth of AgPd nanodendrites on highly purified Au bipyramids with remarkable catalytic performance. *Nanoscale* **2014,** *6*, 12971–12980.

(35) Guo, X.; Zhang, Q.; Sun, Y.; Zhao, Q.; Yang, J. Lateral Etching of Core-Shell Au@Metal Nanorods to Metal-Tipped Au Nanorods with Improved Catalytic Activity. *ACS Nano* **2012,** *6*, 1165–1175.

(36) Zeng, J.; Zhang, Q.; Chen, J.; Xia, Y. A Comparison Study of the Catalytic Properties of Au-Based Nanocages, Nanoboxes, and Nanoparticles. *Nano Lett.* **2010,** *10*, 30–35.

(37) Lim, B.; Jiang, M.; Camargo, P. H. C.; Cho, E. C.; Tao, J.; Lu, X.; Zhu, Y.; Xia, Y. Pd-Pt Bimetallic Nanodendrites with High Activity for Oxygen Reduction. *Science* **2009,** *324*, 1302–1305.

(38) Wang, F.; Cheng, S.; Bao, Z.; Wang, J. Anisotropic Overgrowth of Metal Heterostructures Induced by a Site-Selective Silica Coating. *Angew. Chem. Int. Ed.* **2013,** *52*, 10344–10348.

(39) Huang, J.; Zhu, Y.; Lin, M.; Wang, Q.; Zhao, L.; Yang, Y.; Yao, K. X.; Han, Y. Site-Specific Growth of Au-Pd Alloy Horns on Au Nanorods: A Platform for Highly Sensitive Monitoring of Catalytic Reactions by Surface Enhancement Raman Spectroscopy. *J. Am. Chem. Soc.* **2013,** *135*, 8552–8561.

(40) McEachran, M.; Keogh, D.; Pietrobon, B.; Cathcart, N.; Gourevich, I.; Coombs, N.; Kitaev, V. Ultrathin Gold Nanoframes through Surfactant-Free Templating of Faceted Pentagonal Silver Nanoparticles. *J. Am. Chem. Soc.* **2011,** *133*, 8066–8069.

(41) Zhou, L.; Liu, Z. K.; Zhang, H.; Cheng, S.; Fan, L. J.; Ma, W. L. Site-specific growth of AgPd nanodendrites on highly purified Au bipyramids with remarkable catalytic performance. *Nanoscale* **2014,** *6*, 12971–12980.

(42) Millstone, J. E.; Park, S.; Shuford, K. L.; Qin, L. D.; Schatz, G. C.; Mirkin, C. A. Observation of a quadrupole plasmon mode for a colloidal solution of gold nanoprisms. *J. Am. Chem. Soc.* **2005,** *127*, 5312–5313.

(43) Millstone, J. E.; Wei, W.; Jones, M. R.; Yoo, H.; Mirkin, C. A. Iodide ions control seed-mediated growth of anisotropic gold nanoparticles. *Nano Lett.* **2008,** *8*, 2526–2529.

(44) Kim, J.; Hong, S.; Jang, H.-J.; Choi, Y.; Park, S. Influence of iodide ions on morphology of silver growth on gold hexagonal nanoplates. *J. Colloid Interface Sci.* **2013,** *389*, 71–76.

(45) Chung, P.-J.; Lyu, L.-M.; Huang, M. H. Seed-Mediated and Iodide-Assisted Synthesis of Gold Nanocrystals with Systematic Shape Evolution from Rhombic Dodecahedral to Octahedral Structures. *Chem. Eur. J.* **2011,** *17*, 9746–9752.

(46) Wu, H.-L.; Kuo, C.-H.; Huang, M. H. Seed-Mediated Synthesis of Gold Nanocrystals with Systematic Shape Evolution from Cubic to Trisoctahedral and Rhombic

50

Dodecahedral Structures. *Langmuir* **2010,** *26*, 12307–12313.

(47)   Vieira, K. L.; Peters, D. G. Voltammetric Behavior of Tertiary Butyl Bromide at Mercury Electrodes in Dimethylformamide. *J. Electroanal. Chem.* **1985,** *196*, 93–104.

(48)   Foley, M. P.; Du, P.; Griffith, K. J.; Karty, J. A.; Mubarak, M. S.; Raghavachari, K.; Peters, D. G. Electrochemistry of Substituted Salen Complexes of Nickel(II): Nickel(I)-catalyzed Reduction of Alkyl and Acetylenic Halides. *J. Electroanal. Chem.* **2010,** *647*, 194–203.

(49)   Marple, L. W. Reference electrode for anhydrous dimethylformamide. *Anal. Chem.* **1967,** *39*, 844–846.

(50)   Manning, C. W.; Purdy, W. C. Reference electrode for electrochemical studies in dimethylformamide. *Anal. Chim. Acta* **1970,** *51*, 124–126.

(51)   Hall, J. L.; Jennings, P. W. Modification of the preparation of a cadmium amalgam reference electrode for use in N,N-dimethylformamide. *Anal. Chem.* **1976,** *48*, 2026–227.

(52)   Vanalabhpatana, P.; Peters, D. G. Catalytic reduction of 1,6-dihalohexanes by nickel(I) salen electrogenerated at glassy carbon cathodes in dimethylformamide. *J. Electrochem. Soc.* **2005,** *152*, E222–E229.

(53)   Bharti, S. K.; Roy, R. Quantitative 1H NMR spectroscopy. *Trends Anal. Chem.; TrAC* **2012,** *35*, 5–26.

(54)   Pritts, W. A.; Vieira, K. L.; Peters, D. G. Quantitative determination of volatile products formed in electrolyses of organic compounds. *Anal. Chem.* **1993,** *65*, 2145–2149.

(55)   Magana, S. M.; Quintana, P.; Aguilar, D. H.; Toledo, J. A.; Angeles-Chavez, C.; Cortes, M. A.; Leon, L.; Freile-Pelegrin, Y.; Lopez, T.; Torres Sanchez, R. M. Antibacterial activity of montmorillonites modified with silver. *J. Mol. Catal. A: Chem.* **2008,** *281*, 192–199.

(56)   Wang, Z.-L.; Yan, J.-M.; Wang, H.-L.; Ping, Y.; Jiang, Q. Pd/C Synthesized with Citric Acid: An Efficient Catalyst for Hydrogen Generation from Formic Acid/Sodium Formate. *Sci. Rep.* **2012,** *2:598*.

(57)   Grammatikopoulos, P.; Cassidy, C.; Singh, V.; Sowwan, M. Coalescence-induced crystallisation wave in Pd nanoparticles. *Sci. Rep.* **2014,** *4*:5779.

(58)   Millstone, J. E.; Hurst, S. J.; Metraux, G. S.; Cutler, J. I.; Mirkin, C. A. Colloidal Gold and Silver Triangular Nanoprisms. *Small* **2009,** *5*, 646–664.

(59)   Kelly, K. L.; Coronado, E.; Zhao, L. L.; Schatz, G. C. The optical properties of metal nanoparticles: The influence of size, shape, and dielectric environment. *J. Phys. Chem. B* **2003,** *107*, 668–677.

(60)   Xue, C.; Mirkin, C. A. pH-switchable silver nanoprism growth pathways. *Angew. Chem. Int. Ed.* **2007,** *46*, 2036–2038.

(61)   Sherry, L. J.; Jin, R.; Mirkin, C. A.; Schatz, G. C.; Van Duyne, R. P. Localized surface plasmon resonance spectroscopy of single silver triangular nanoprisms. *Nano Lett.* **2006,** *6*, 2060–2065.

(62)   Perez-Juste, J.; Liz-Marzan, L. M.; Carnie, S.; Chan, D. Y. C.; Mulvaney, P. Electric-field-directed growth of gold nanorods in aqueous surfactant solutions. *Adv. Funct. Mater.* **2004,** *14*, 571–579.

51

(63) Herrero, E. B., L. J.; Abruña, H. D. Underpotential deposition at single crystal surfaces of Au, Pt, Ag and other materials. *Chem. Rev.* **2001,** *101*, 1897–1930.

(64) Tian, Z.; Huarong, N.; Bain, T. S.; Haiyun, L.; Mengmeng, C.; Snoeyenbos-West, O. L.; Franks, A. E.; Nevin, K. P.; Russell, T. P.; Lovley, D. R. Improved cathode materials for microbial electrosynthesis. *Energy Environ. Sci.* **2013,** *6*, 217–224.

(65) Sun, Y.; Xia, Y. Shape-Controlled Synthesis of Gold and Silver Nanoparticles. *Science* **2002,** *298*, 2176–2179.

(66) Zhang, Q.; xie, J.; Lee, J. Y.; Zhang, J.; Boothroyd, C. Synthesis of Ag@AgAu metal core/alloy shell bimetallic nanoparticles with tunable shell compositions by a galvanic replacement reaction. *Small* **2008,** *4*, 1067–1071.

(67) Camargo, P. H. C.; Xiong, Y.; Ji, L.; Zuo, J. M.; Xia, Y. Facile synthesis of tadpole-like nanostructures consisting of Au heads and Pd tails. *J. Am. Chem. Soc.* **2007,** *129*, 15452–15453.

(68) Yin, Y.; Erdonmez, C.; Aloni, S.; Alivisatos, A. P. Faceting of nanocrystals during chemical transformation: From solid silver spheres to hollow gold octahedra. *J. Am. Chem. Soc.* **2006,** *128*, 12671–12673.

(69) Zhang, H.; Jin, M.; Wang, J.; Li, W.; Camargo, P. H. C.; Kim, M. J.; Yang, D.; Xie, Z. Synthesis of Pd-Pt bimetallic nanocrystals with a concave structure through a bromide-induced galvanic replacement reaction. *J. Am. Chem. Soc.* **2011,** *133*, 6078–6089.

(70) Kortlever, R. P., I.; Koper, S.; Koper, M. T. M. Electrochemical CO2 Reduction to Formic Acid at Low Overpotential and with High Faradaic Efficiency on Carbon-Supported Bimetallic Pd–Pt Nanoparticles. *ACS Catal.* **2015,** *5,* 3916-3923.

(71) Humphrey, J. J. L.; Plana, D.; Celorrio, V.; Sadasivan, S.; Tooze, R. P.; Rodríguez, P.; and Fermín, D. J. Electrochemical Reduction of Carbon Dioxide at Gold-Palladium Core–Shell Nanoparticles: Product Distribution versus Shell Thickness. *ChemCatChem* **2016,** *8*, 952–960.

(72) Chang, J.; Feng, L.; Liu, C.; Xing, W.; Hu, X. An Effective Pd–Ni2P/C Anode Catalyst for Direct Formic Acid Fuel Cells. *Angew. Chem. Int. Ed.* **2013,** *53*, 122–126.

(73) Kas, R. H., K. K.; Kortlever, R.; de Wit, P.; Milbrat, A.; Luiten-Olieman, M. W. J.; Benes, N. E.; Koper, M. T. M.; Mul, G. Three-dimensional porous hollow fibre copper electrodes for efficient and high-rate electrochemical carbon dioxide reduction. *Nat. Commun.* **2016,** *7*:10748.

(74) Klinkova, A.; De Luna, P.; Dinh, C.; Voznyy, O.; Larin, E. M.; Kumacheva, E.; Sargent, E. H. Rational Design of Efficient Palladium Catalysts for Electroreduction of Carbon Dioxide to Formate. *ACS Catal.* **2016,** *6*, 8115–8120.

(75) Scialdone, O.; Galia, A.; Lo Nero, G.; Proietto, F.; Sabatino, S.; Schiavo, B. Electrochemical reduction of carbon dioxide to formic acid at a tin cathode in divided and undivided cells: effect of carbon dioxide pressure and other operating parameters. *Electrochim. Acta* **2016,** *199*, 332–341.

(76) Kumar, B.; Atla, V.; Brian, J. P.; Kumari, S.; Nguyen, T. Q.; Sunkara, M.; Spurgeon, J. M. Reduced SnO_2 Porous Nanowires with a High Density of Grain Boundaries as Catalysts for Efficient Electrochemical CO_2-into-HCOOH Conversion. *Angew. Chem. Int. Ed.* **2017,** *56*, 3645–3649.

52

(77) Gue, S. Z., S.; Gao, J.; Zhu, C.; Wu, X.; Fu, Y.; Huang, H.; Liu, Y.; Kang, Z. Cu-CDots nanocorals as electrocatalyst for highly efficient CO2 reduction to formate. *Nanoscale* **2017,** *9*, 298–304.

(78) Kern, D. M. The hydration of carbon dioxide. *J. Chem. Educ.* **1960,** *37*, 14–23.

(79) Min, X. K., M. W. Pd-Catalyzed Electrohydrogenation of Carbon Dioxide to Formate: High Mass Activity at Low Overpotential and Identification of the Deactivation Pathway. *J. Am. Chem. Soc.* **2015,** *137*, 4701–4708.

(80) Spichiger-Ulmann, M.; Augustynski J.; Electrochemical reduction of bicarbonate ions at a bright palladium cathode. *J. Chem. Soc., Faraday Transactions* **1985,** *81*, 713–16.

(81) Lu, X.; Leung, D. Y. C.; Wang, H.; Leung, M. K. H.; Xuan, J. Electrochemical Reduction of Carbon Dioxide to Formic Acid. *Chemelectrochem* **2014,** *1*, 836–849.

(82) Gennaro, A.; Isse, A. A.; Severin, M.; Vianello, E.; Bhugen, I.; Savéant, J. Mechanism of the electrochemical reduction of carbon dioxide at inert electrodes in media of low proton availibility. *J. Chem. Soc., Faraday Trans.* **1996,** *92*, 3963–3968.

(83) Podlovchenko, B. I.; Kolyadko, E. A.; Lu, S. Electroreduction of carbon dioxide on palladium electrodes at potentials higher than the reversible hydrogen potential. *J. Electroanal. Chem.* **1994,** *373*, 185–187.

(84) Chaplin, R. P. S.; Wragg, A. A. Effects of process conditions and electrode material on reaction pathways for carbon dioxide electroreduction with particular reference to formate formation. *J. App. Electrochem.* **2003,** *33*, 1107–1123.

(85) Mistry, H.; Reske, R.; Zeng, Z.; Zhao, Z.-J.; Greeley, J.; Strasser, P.; Cuenya, B. R. Exceptional Size-Dependent Activity Enhancement in the Electroreduction of CO2 over Au Nanoparticles. *J. Am. Chem. Soc.* **2014,** *136*, 16473–16476.

(86) Back, S.; Yeom, M. S.; Jung, Y. Active Sites of Au and Ag Nanoparticle Catalysts for CO2 Electroreduction to CO. *ACS Catal.* **2015,** *5*, 5089–5096.

(87) Freund, H. J.; Roberts, M. W. Surface chemistry of carbon dioxide. *Surf. Sci. Rep.* **1996,** *25*, 225–273.

(88) Jewell, L. L.; Burtron, H. D. Review of absorption and adsorption in the hydrogen-palladium system. *Appl. Catal., A* **2006,** *310*, 1–15.

(89) Johansson, M. S., E.; Nielson, G.; Murphy, S.; Nielson, R. M.; Chorkendorff, I. Hydrogen adsorption on palladium and palladium hydride at 1 bar. *Surf. Sci.* **2010,** *604*, 718–729.

(90) Grden, M.; Paruszewska, A.; Czerwinski, A. Electrosorption of carbon dioxide on Pd-Pt alloys. *J. Electroanal. Chem.* **2001,** *502*, 91–99.

(91) Hong, W.; Wang, J.; Wang, E. K. Dendritic Au/Pt and Au/PtCu Nanowires with Enhanced Electrocatalytic Activity for Methanol Electrooxidation. *Small* **2014,** *10*, 3262–3265.

(92) Tomita, Y. T., S.; Koga, O.; Hori, Y. Electrochemical Reduction of Carbon Dioxide at a Platinum Electrode in Acetonitrile-Water Mixtures. *J. Electrochem. Soc.* **2000,** *147*, 4164–4167.

(93) Homel, M.; Gur, T. M.; Koh, J. H.; Virkar, A. V. Carbon monoxide-fueled solid oxide fuel cell. *J. Power Sources* **2010,** *195*, 6367–6372.

(94) Hori, Y. Electrochemical CO_2 Reduction on Metal Electrodes. *Modern Aspects of Electrochemistry* **2008** *42*, 89–189.

(95)　Ding, C.; Li, A.; , Lu, S.; Zhang, H.; Li, C. In Situ Electrodeposited Indium Nanocrystals for Efficient CO2 Reduction to CO with Low Overpotential. *ACS Catal.* **2016,** *6*, 6438–6443.

(96)　Asadi, M.; Kim, K.; Liu, C.; Addepalli, A. V.; Abbasi, P.; Yasaei, P.; Phillips, P.; Behranginia, A.; Cerrato, J. M.; Haasch, R.; Zapol, P.; Kumar, B.; Klie, R. F.; Abiade. J.; Curtiss, L. A.; Salehi-Khojin, A. Nanostructured transition metal dichalcogenide electrocatalysts for CO2 reduction in ionic liquid. *Science* **2016,** *353*, 467–470.

(97)　Abbasi, P.; Asadi, M.; Liu, C.; Sharifi-Asl, S.; Sayahpour, B.; Behranginia, A.; Zapol, P.; Shahbazian-Yassar, R.; Curtiss, L. A.; Salehi-Khojin, A. Tailoring the Edge Structure of Molybdenum Disulfide toward Electrocatalytic Reduction of Carbon Dioxide. *ACS Nano* **2017,** *11*, 453–460.

1
2
3
4
5
6
7
8
9
10
11
12
13
14
15
16
17
18
19
20
21
22
23
24
25
26
27
28
29
30
31
32
33
34
35
36
37
38
39
40
41
42
43
44
45
46
47
48
49
50
51
52
53
54
55
56
57
58
59
60

54

TOC Graphic

AgPd nanodendrite-tipped Au prism for CO_2 electro-reduction

CO_2 — Low overpotential in aqueous electrolyte → HCOOH

CO_2 — High efficiency in organic electrolyte → CO

Au   Ag   Pd   50 nm

55